ELSEVIER

Contents lists available at ScienceDirect

Computers and Fluids

journal homepage: www.elsevier.com/locate/compfluid



Application of projection and immersed boundary methods to simulating heat and mass transport in membrane distillation



Jincheng Lou, Jacob Johnston, Nils Tilton*

Mechanical Engineering, Colorado School of Mines, United States

ARTICLE INFO

Article history:
Received 2 March 2020
Revised 2 August 2020
Accepted 14 August 2020
Available online 1 September 2020

Keywords:
Membrane distillation
Immersed boundary methods
Projection methods
Outlet conditions

ABSTRACT

Membrane distillation is an emerging desalination process with important applications to the energywater nexus. Its performance depends, however, on heat and mass transport phenomena that are uniquely challenging to simulate. Difficulties include two adjacent channel flows coupled by heat and mass transport across a semi-permeable membrane. Within the channels, heat and mass boundary layers interact with the membrane surface and vortical flow structures generated by complicated geometries. The presence of multiple inlets and outlets also complicates the application of mass-conserving outlet conditions. Moreover, even small amounts of outlet noise affect the resolution of important nearmembrane fluid velocities. We show these phenomena can be simulated to second-order spatial and temporal accuracy using finite volume methods with immersed boundaries and projection methods. Our approach includes a projection method that staggers the coupled channel flows and applies Robin boundary conditions to facilitate mass conservation at the outlets. We also develop an immersed boundary method that applies Neumann boundary conditions to second-order spatial accuracy. The methods are verified and validated against manufactured solutions and theoretical predictions of vortex shedding. They are then applied to the simulation of steady and unsteady transport phenomena in membrane distillation. The methods have important applications to the broad field of chemical engineering and deal with longstanding issues in both theoretical and computational fluid dynamics.

© 2020 Elsevier Ltd. All rights reserved.

1. Introduction

Membrane distillation is an emerging method of desalinating wastewaters produced by industry, agriculture, and municipalities [1–3]. Though the method has attracted considerable attention as a means of addressing global water crises, its energy efficiency depends on heat and mass transport phenomena that are poorly understood because they are difficult to simulate or observe experimentally [4]. Challenges include simultaneous heat and mass boundary layers that interact with semi-permeable membranes and unsteady vortical flow structures generated by bluff bodies with complicated geometries. These phenomena occur in small flow channels with gap heights on the order of 1 mm. Membrane distillation systems are also open systems with multiple inlets and outlets that complicate the application of mass-conserving outlet conditions. Even small amounts of outlet noise can also affect the resolution of important near-membrane fluid velocities that are four to five orders-of-magnitude smaller than the largest velocity magnitudes. We show that these compounding phenomena can be successfully simulated to second-order spatial and temporal accuracy using finite volume methods with immersed boundaries and projection methods. Our approach includes the development of a direct-forcing immersed boundary method that applies Neumann conditions to second-order spatial accuracy. Though developed here for membrane distillation, the methods have important applications to the broad field of chemical engineering and deal with long-standing issues in computational fluid dynamics (CFD).

We consider the common arrangement of direct contact membrane distillation (DCMD) sketched in Fig. 1(a). Warm feed solution and cool distilled water flow on opposite sides of a hydrophobic membrane. The temperature difference across the membrane creates a difference in partial vapor pressure that causes water to evaporate from the feed side of the membrane, travel through the pores as vapor, and condense on the distillate side of the membrane. Non-volatile solutes remain in the feed. In comparison to reverse osmosis desalination, DCMD's primary advantage is that it can treat higher concentration feed solutions because it is insensitive to osmotic pressure. Reverse osmosis can only treat NaCl solutions up to approximately 70 g/L, beyond which the required operating pressure becomes economically prohibitive. In contrast, the limit for DCMD is around 300 g/L [5]. DCMD also operates at low

^{*} Corresponding author.

E-mail address: ntilton@mines.edu (N. Tilton).

```
Nomenclature
β
          blockage ratio \beta = D_c/h
          transmembrane temperature difference \Delta T_m = T_m^f
\Delta T_m
          T_m^d (°C)
δ
          membrane thickness (m)
\delta_T
          thermal boundary layer thickness (m). See Eq. (40)
λ
          latent heat of water (J/kg)
          forcing terms added for benchmarking purposes
\mathbf{f}_u, f_T, f_c
n
          unit normal to surfaces
          velocity vector (m/s)
u
\mathbf{u}^*
          provisional velocity vector in projection method
          (m/s). See Eq. (14)
\mathcal{D}
          mass diffusivity (m<sup>2</sup>/s)
          dynamic viscosity (Pa s)
\mu
          kinematic viscosity (m<sup>2</sup>/s)
ν
v^f, v^d
          kinematic viscosity of feed and distillate fluid (m<sup>2</sup>/s)
φ
          intermediate variable used in projection method.
          See Eq. (15)
          density (kg/m<sup>3</sup>)
          density of feed and distillate fluid (kg/m³)
          non-dimensional temperature. See equation (39)
a, b
          coefficients in Robin boundary conditions. See
          Eq. (26)
          water activity
a_w
          vapor permeability (kg/m<sup>2</sup> sPa)
В
b
          NaCl molality (mol/kg)
          concentration (g/L)
С
          C(x) = \cos(x). See Eq. (21)
C(x)
          membrane surface concentration (g/L)
c_m
          specific heat capacity (I/kg K)
c_p
          feed concentration (g/L)
C_{in}
          normal distance from a forcing point to the surface.
          See Fig. 11
D_c
          cylinder diameter (m). See Fig. 2
DCMD
          direct Contact Membrane Distillation
dt
          numerical time step (s)
Err_N
          spatial error. See Eq. (22)
Err_t
          temporal error. See Eq. (23)
          forcing point in immersed boundary method. See
f
          Fig. 10
          dominant frequency of vortex shedding
f_c
h
          channel height (m)
          transmembrane mass flux (kg/m<sup>2</sup> s)
jν
k
          thermal conductivity (W/m °C)
          membrane thermal conductivity (W/m °C)
k_m
          channel length (m)
L
          fictitious points used to apply immersed Neumann
n
          conditions. See Fig. 11
          pressure (Pa)
р
p_m^f, p_m^d
          vapor pressure on the feed and distillate side of
          membrane (Pa)
psat
          water vapor saturation pressure (Pa)
          transmembrane heat conduction (W/m<sup>2</sup>)
q_c
          Reynolds number Re = U_{in}h/v
Re
Re_c
          critical Reynolds number for transition to vortex
          shedding
          distillate Reynolds number Re_d = U_{in}h/v^d
Re_d
          feed Reynolds number Re_f = U_{in}h/v^f
Re_f
          surface point used in immersed boundary method.
          See Fig. 11
S(x)
          S(x) = \sin(x). See Eq. (21)
          critical Strouhal number St_c = f_c D_c / U_{in}
St_c
```

```
Τ
          temperature (°C)
          time (s)
          membrane surface temperature on the feed and dis-
          tillate side (°C)
T_{in}^f, T_{in}^d

T_m^d

T_m^f
          feed and distillate inlet temperature (°C)
          membrane distillate surface temperature (°C)
          membrane feed surface temperature (°C)
TVD
          total variation diminishing
u, v
          velocity component along x and y coordinates (m/s)
U_{in}
          inlet velocity (m/s)
          local transmembrane velocity v_m = j_v/\rho^f measured
v_m
          from feed side of membrane (m/s)
x, y
          cartesian coordinates (m)
          denotes a boundary condition applied on the feed
v^+
          surface of the membrane
y^{-}
          denotes a boundary condition applied on the distil-
          late surface of the membrane
          cylinder position relative to the membrane surface
y_c
          (m). See Fig. 2
          y_f = y + 1/2. See Eq. (21)
y_d
          y_f = y - 1/2. See Eq. (21)
\| \|_{\infty}
          Infinity norm
```

feed temperatures between 40 to 90 $^{\circ}\text{C}$ readily produced by renewable energy and industrial heat.

DCMD is strongly influenced by two phenomena called temperature and concentration polarization [3], sketched in Fig. 1(a). Temperature polarization refers to the formation of thermal boundary layers along the feed and distillate surfaces of the membrane due to heat transfer through the membrane, as sketched in Fig. 1(a). This reduces the temperature difference ΔT_m and partial vapor pressure difference across the membrane, and consequently the rate of vapor production. Concentration polarization refers to the formation of a concentration boundary layer along the feed surface of the membrane. This occurs because solutes are advected toward the membrane, where they accumulate because they are non-volatile. Concentration polarization reduces the partial vapor pressure of the feed solution on the membrane, and consequently reduces vapor production. Concentration polarization also causes mineral scaling, which is the precipitation of salts onto the membrane surface. This blocks the membrane surface and causes permanent membrane damage. Understanding polarization is further complicated by the presence of membrane spacers. Spacers are mesh-like materials that separate and support tightly packed membrane sheets in filtration systems, as sketched in Fig. 1(b). Spacers are present in both the feed and distillate channels of DCMD systems, where they induce three-dimensional mixing and generate regions of preferential solute accumulation and precipita-

Numerous studies have made important progress in simulating membrane distillation [4,6,7]. We nevertheless find three persistent challenges. First, the accurate prediction of polarization requires the simultaneous simulation of the coupled feed channel, transmembrane flow, and distillate channel. This complicates a fundamental issue that arises in the simulation of almost all incompressible fluid flows. The pressure field in an incompressible fluid flow ensures that the velocity field remains divergence free. Because the pressure lacks an evolution equation, the numerical difficulty is to somehow determine the pressure without solving the fully coupled Navier-Stokes and continuity equations simultaneously. For unsteady fluid flows, the most popular solution to this challenge are projection methods based on pioneering work of Chorin [8] and Temam [9]. Unfortunately, the application of projection methods to open systems with multiple inlets and outlets

Fig. 1. (a) Sketch (not to scale) of the 2-D plate-and-frame DCMD system considered in this study. See description in text. The arrows depict streamlines. The membrane is shaded grey, and concentration polarization is shown by the solid dots accumulated near the membrane. The temperature profile shows the effects of temperature polarization. (b) Sketch (not to scale) of a membrane spacer.

is not trivial, and to our knowledge, they have never been applied to DCMD systems.

A second challenge arises because simulations of membrane separation systems currently rely on body-fitted grids. For complicated spacer geometries, the time required to generate such grids becomes so onerous that studies must limit the number of spacer geometries that can be considered [10]. The third challenge arises because the flow regime within DCMD systems is not fully understood. Though studies show that with increasing Reynolds number, the flow transitions from steady flow to laminar vortex shedding and perhaps turbulence [7,11–18], these transitions are not well understood. In fact, though spacers are often called "turbulence promoters," it is not clear whether DCMD systems typically operate in turbulent regimes.

We address these issues using a combination of finite volume, projection, and immersed boundary methods. We first show that unsteady flow in the coupled feed and distillate channels can be simulated using a projection method that solves the two channel flows sequentially, rather than simultaneously. The projection method is also derived for general Robin conditions on the numerical domain to improve the application of outlet conditions. Noise at the inlet and outlet is also attenuated using a Total Variation Diminishing (TVD) scheme and a set of "buffer cells" appended to the inlets and outlets of the two channels. We next develop an immersed boundary method that applies no-slip (Dirichlet) and no-flux (Neumann) boundary conditions on spacer surfaces to second-order spatial accuracy. Finally, we combine these methods to investigate polarization and transition to vortex shedding in DCMD systems. The remaining article is organized as follows. Section 2 presents the geometry and governing equations. Sections 3 and 4 present the projection and immersed boundary methods, respectively. Section 5 simulates vortex shedding in a DCMD system. Section 6 presents our conclusions.

2. Geometry and governing equations

We consider a 2-D flat-sheet membrane system (called a "plateand-frame" system) with feed and distillate channels of length L and height h, as sketched in Fig. 2. NaCl solution enters the feed channel with temperature T_{in}^f , concentration C_{in} , and mean velocity U_{in} . Pure water enters the distillate channel with temperature T_{in}^d and the same mean velocity U_{in} as in the feed channel. Though Fig. 2 shows the membrane as a shaded region about y = 0, we model transmembrane heat and mass transport using effective interface conditions that couple the feed $(0 \le y \le h)$ and distillate $(-h \le y \le 0)$ channels. To investigate vortex shedding, we consider cylindrical spacer filaments of diameter D_c , placed a distance y_c from the membrane. Though spacers are inherently 3D, we focus first on idealized spacers because their hydrodynamic stability is far better understood [19,20]. Their simplicity also allows us to perform a parametric study and complementary experimental study, both ongoing in our group. In contrast, industrial spacers are typically composed of two layers of extruded polypropylene filaments oriented roughly 45° to the downstream flow direction, as

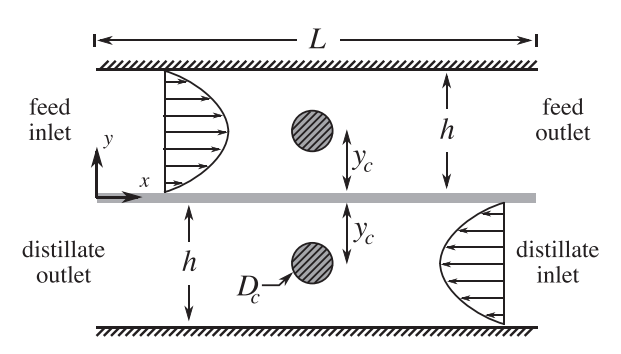


Fig. 2. Sketch (not to scale) of the 2-D plate-and-frame DCMD system considered in this study. See description in text.

sketched in Fig. 1(b). For more discussion of the various spacer designs, we refer to the review of Haidari et al. [21].

Fluid flow in the feed and distillate channels is governed by the incompressible continuity and Navier-Stokes equations for Newtonian fluids,

$$\nabla \cdot \mathbf{u} = 0, \quad \rho \left[\frac{\partial \mathbf{u}}{\partial t} + (\mathbf{u} \cdot \nabla) \mathbf{u} \right] = -\nabla p + \mu \nabla^2 \mathbf{u} + \mathbf{f}_u, \tag{1}$$

where $\mathbf{u} = [u \ v]$, p, ρ and μ are the fluid velocity, pressure, density, and viscosity, respectively. The force \mathbf{f}_u is added for benchmarking in Section 3.1. In each channel, we neglect density variations with temperature and concentration, because the maximum density variation is within 3%. In each channel, we set the density to that evaluated at the inlet temperature and concentration. Though buoyancy-driven convection can be included using the Boussinesq approximation, we leave that topic to a future dedicated study.

Heat and NaCl transport are governed by the energy and advection-diffusion equations,

$$\rho c_p \left[\frac{\partial T}{\partial t} + (\mathbf{u} \cdot \nabla) T \right] = k \nabla^2 T + f_T, \tag{2}$$

$$\frac{\partial c}{\partial t} + (\mathbf{u} \cdot \nabla)c = \mathcal{D}\nabla^2 c + f_c, \tag{3}$$

where T is the temperature, c is the concentration, c_p is the fluid heat capacity, and \mathcal{D} is the effective mass diffusivity. The source terms f_T and f_c are again added for benchmarking. For the systems considered in the current study, we found that variations of μ , k, \mathcal{D} , and c_p with temperature and concentration had an order 1% effect on our simulations. Though they can be included using the procedure in Lou et al. [4], we neglect them here to simplify our presentation.

Assuming the impermeable plates and spacers are insulated, we apply the following no-slip, no-penetration, and no-flux boundary conditions,

$$\mathbf{u} = \mathbf{n} \cdot \nabla c = \mathbf{n} \cdot \nabla T = 0, \tag{4}$$

where **n** is the unit normal to the surface. We also apply the noslip condition (u = 0) to the membrane surface (y = 0). Though usually neglected, and not considered here, slip due to hydrophobicity can be modeled using the Navier slip condition [22]. At the channel inlets, we apply parabolic laminar velocity profiles $u_{in}(y)$ with the desired uniform temperature T_{in} , and concentration C_{in} ,

$$u = u_{in}(y), \quad v = 0, \quad T = T_{in}, \quad c = C_{in}.$$
 (5)

We consider two popular channel outlet conditions [23],

$$\frac{\partial f}{\partial x} = 0, \quad \frac{\partial f}{\partial t} + U_{in} \frac{\partial f}{\partial x} = 0,$$
 (6)

where f denotes \mathbf{u} , c, and T. The first condition is a Neumann condition, while the second is a convective condition.

The channel flows are coupled by heat and vapor transport through the membrane. We first note that mass conservation across the membrane requires

$$\rho^{f} v \bigg|_{y=0^{+}} = \rho^{d} v \bigg|_{y=0^{-}} = j_{v}, \tag{7}$$

where j_{ν} is the transmembrane vapor mass flux, and ρ^f and ρ^d are the liquid densities in the feed and distillate channels, respectively. The superscripts "+" and "–" denote evaluation of ν on the feed and distillate sides of the membrane, respectively. Assuming no solutes pass through the membrane, salt diffusion and advection normal to the feed membrane surface must sum to zero,

$$vc\Big|_{y=0^+} - \mathcal{D}\frac{\partial c}{\partial y}\Big|_{y=0^+} = 0.$$
 (8)

MD membranes are typically fibrous materials with pore-spaces on the order of 1–10 μ m. Experiments [4,24] show that transmembrane heat and vapor transport is well approximated on a macroscopic level using a popular model proposed by Schofield et al. [25]. The model begins by assuming the vapor mass flux j_v is linearly proportional to the transmembrane vapor pressure difference,

$$j_{\nu} = -B(p_m^f - p_m^d), \tag{9}$$

where p_m^f and p_m^d are the partial vapor pressures on the feed and distillate sides of the membrane, respectively, and B is the membrane's vapor permeability, which is determined experimentally [4,25,26]. We evaluate p_m^f and p_m^d as the product of the vapor saturation pressure P^{sat} and water activity a_w ,

$$p_m = a_w P^{sat}, \quad P^{sat} = \exp\left(23.238 - \frac{3841}{T_m - 45}\right),$$
 (10)

where P^{sat} is determined using the Antoine equation [27] and T_m is the local temperature on the membrane surface. The activity is determined from the expression $a_w = 1 - 0.03112b - 0.001482b^2$ [28], where b is the NaCl molality (mol/kg). This expression is valid from zero salinity to saturation.

Heat transport through MD membranes occurs due to conduction through the membrane material and combined conduction and advection in the vapor. The Schofield model [25] approximates transmembrane heat transport due to conduction (q_c) and advection (q_v) as

$$q_c = -\frac{k_m}{\mathcal{S}} (T_m^f - T_m^d), \quad q_\nu = j_\nu \lambda, \tag{11}$$

where δ and k_m are the membrane thickness and thermal conductivity, respectively, T_m^f and T_m^d are the local temperatures on the feed and distillate sides of the membrane, respectively, and λ is the latent heat per unit mass. Following common practice, we determine the ratio k_m/δ by fitting to experiments [4]. Conservation of energy principles for phase changes at the liquid-vapor interfaces [29] produce the temperature conditions,

$$-k\frac{\partial T}{\partial y}\bigg|_{y=0^{\pm}} = j_{\nu}\lambda - \frac{k_{m}}{\delta} \Big(T\big|_{y=0^{+}} - T\big|_{y=0^{-}}\Big). \tag{12}$$

Though well established in the membranes community, the subtleties of how conditions (12) account for phase-change are provided in Appendix A. Following common practice, we set λ to the average of the two inlet values. The thermal conductivity k on the left-hand-side is set to the feed value when $y=0^+$, and the distillate value when $y=0^-$.

3. Simulation of the coupled channel flows

This section presents our simulation of the coupled channels without spacers. The primary challenge arises from the membrane and outlet conditions. We address these issues separately in Sections 3.1 and 3.2, below. We discretize the governing equations spatially using standard second-order finite volume methods on a non-uniform staggered grid [30]. Details are presented in Appendix B.

3.1. Application of membrane conditions

To delay our discussion of outlet conditions, suppose we simulate the coupled channel flows in Fig. 2 with the velocity, temperature, and concentration prescribed at the outlets. To implement the membrane conditions, we develop a projection method that staggers the solution of momentum transport in the coupled channel flows. We first discretize all equations semi-implicitly in time using the Crank-Nicolson method for linear terms and Adams-Bashforth methods for nonlinear terms, as below for the Navier-Stokes equation.

$$\rho \frac{\mathbf{u}^{n+1} - \mathbf{u}^n}{dt} + \frac{3}{2} \mathbf{N} \mathbf{L}^n - \frac{1}{2} \mathbf{N} \mathbf{L}^{n-1} = -\nabla p^{n+1/2} + \frac{\mu}{2} \nabla^2 (\mathbf{u}^{n+1} + \mathbf{u}^n),$$
(13)

where dt is the time step, the superscript n denotes time t = n dt, and $\mathbf{NL}^n = \rho(\mathbf{u}^n \cdot \nabla)\mathbf{u}^n$. We enforce incompressibility using the projection method of Bell et al., [31]. We first compute a provisional velocity \mathbf{u}^* by solving Eq. (13) with the pressure from the previous time step,

$$\rho \frac{\mathbf{u}^* - \mathbf{u}^n}{dt} + \frac{3}{2} \mathbf{N} \mathbf{L}^n - \frac{1}{2} \mathbf{N} \mathbf{L}^{n-1} = -\nabla p^{n-1/2} + \frac{\mu}{2} \nabla^2 (\mathbf{u}^* + \mathbf{u}^n). \quad (14)$$

Subtracting Eq. (14) from Eq. (13), produces the relation

$$\mathbf{u}^{n+1} = \mathbf{u}^* - \frac{dt}{\rho} \nabla \phi, \tag{15}$$

where $\phi=p^{n+1/2}-p^{n-1/2}$ is sometimes called the "pseudopressure." Relation (15) neglects the viscous term $\mu(\nabla^2 \mathbf{u}^{n+1}-\nabla^2 \mathbf{u}^*)/2$, which has a negligible impact [32]. Taking the divergence of Eq. (15) and applying incompressibility produces a Poisson equation for ϕ ,

$$\nabla^2 \phi = \frac{\rho}{dt} \nabla \cdot \mathbf{u}^*. \tag{16}$$

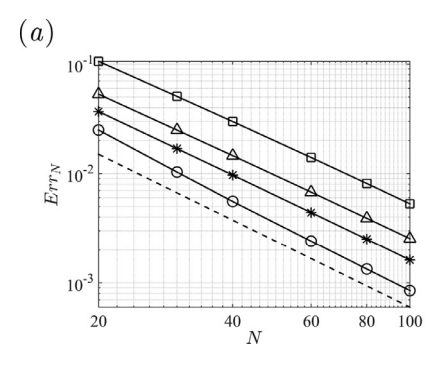
Selecting boundary conditions for \mathbf{u}^* and ϕ is a topic of considerable discussion [23,32–35]. Suppose we wish to prescribe the velocity $\mathbf{u}^{n+1} = \mathbf{g}(y)$ on the boundary x = 0. It now well established that at x = 0, one can set $\mathbf{u}^* = \mathbf{g}$ and $\partial \phi / \partial x = 0$. These conditions arise from Eq. (15), which requires

$$\left. \frac{\partial \phi}{\partial x} \right|_{x=0} = \frac{\rho}{dt} \left[u^* - u^{n+1} \right]_{x=0}. \tag{17}$$

More generally, if one wishes to set the velocity $\mathbf{u}^{n+1} = \mathbf{g}$ on some boundary with unit normal $\hat{\mathbf{n}}$, one applies the conditions

$$\mathbf{u}^* = \mathbf{g}, \quad \widehat{\mathbf{n}} \cdot \nabla \phi = 0. \tag{18}$$

Note that to ensure mass conservation, the above Poisson equation and boundary conditions must be derived using the spatially discretized Navier-Stokes and continuity equations, as demonstrated in Appendix B.



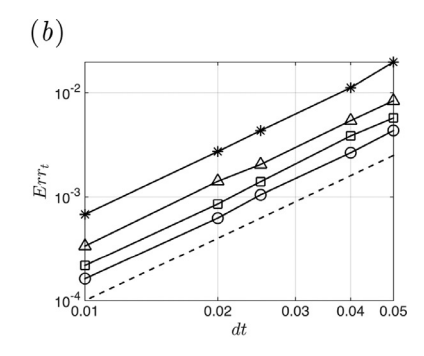


Fig. 3. Error results for u (squares), v (asterisks), T (triangles), c (circles). (a) Err_N vs. N. The dashed line shows $1/N^2$. (b) Err_t vs. dt. The dashed line shows dt^2 .

To apply the above projection method to our coupled channel flows, we discretize the membrane conditions semi-implicitly in time to solve the flow fields in each channel sequentially, rather than simultaneously. Each time step begins by solving the heat and advection-diffusion Eqs. (2) and (3) in the channels by discretizing the membrane conditions (8) and (12) as

$$D\frac{\partial c^{n+1}}{\partial y}\bigg|_{y=0^{+}} = \overline{vc}\bigg|_{y=0^{+}},\tag{19}$$

$$-k\frac{\partial T^{n+1}}{\partial y}\bigg|_{y=0^{\pm}} = -\frac{k_m}{\delta} \left(\overline{T}\big|_{y=0^{+}} - \overline{T}\big|_{y=0^{-}}\right) + \overline{j_{\nu}}\lambda,\tag{20}$$

where the overline denotes the Adams-Bashforth approximation $\overline{vc} = 2v^nc^n - v^{n-1}c^{n-1}$. This allows us to solve for c^{n+1} and T^{n+1} in each channel sequentially. We then compute the vapor flux j_v^{n+1} using Eqs. (9) and (10), and solve the Navier-Stokes equations in both channels sequentially.

We verify the spatial and temporal accuracy of our coupled channel flow solver with respect to the manufactured analytical solution

$$\begin{bmatrix} u_f \\ v_f \\ p_f \\ T_f \\ c_f \end{bmatrix} = \begin{bmatrix} -S(x)C(\pi y_f/2) \\ \frac{2}{\pi}C(x)S(\pi y_f/2) \\ S(x)S(y_f) \\ \frac{3}{\pi}C(x)y_f^2 \\ S(x)y_f^2 \end{bmatrix} C(\omega t),$$

$$\begin{bmatrix} u_d \\ v_d \\ p_d \\ T_d \end{bmatrix} = \begin{bmatrix} S(x)C(\pi y_d/2) \\ -\frac{2}{\pi}C(x)S(\pi y_d/2) \\ S(x)S(y_d) \\ \frac{1}{\pi}C(x)y_d^2 \end{bmatrix} C(\omega t),$$
(21)

where $y_f=y-1/2,\ y_d=y+1/2,\ C=\cos$ and $S=\sin$. The subscripts f and d denote the solutions used in the feed and distillate channels, respectively. The solution assumes $h=2,\ L=\pi,\ \rho=\mu=c_p=k=k_m/\delta=B=\lambda=a_w=1,$ and replaces the Antoine Eq. (10) with $P^{sat}=T_m$. This produces the transmembrane temperature difference $T_m^f-T_m^d=(2/\pi)\cos(x)\cos(\omega t),$ membrane concentration $c_m=\sin(x)\cos(\omega t),$ and transmembrane velocity $v_m=-(2/\pi)\cos(x)\cos(\omega t).$ The solution satisfies the governing equations with the addition of appropriate forcing terms to Eqs. (1)–(3) and conditions (8) and (12). On the inlets, outlets, and plates, we set $\mathbf{u},\ T,$ and c to the test solution. We use a uniform grid in the c-direction and a non-uniform grid in the c-direction, given by Eq. (67) of Appendix c.

We test the spatial convergence by setting $\omega=0$ and integrating from $\mathbf{u}^0=p^0=T^0=c^0=0$ to steady state using N^2 finite-volumes in each channel (N volumes in each direction). We then measure the relative error of each field as,

$$Err_N = \frac{\|f_e - f_N\|_{\infty}}{\|f_e\|_{\infty}},\tag{22}$$

where f_e and f_N are the exact and numerical solutions, respectively. We test the temporal convergence by setting $\omega=2\pi$ and integrating from t=0 to t=1 using exact initial conditions. We then compute the error

$$Err_{t} = \frac{\|f_{e} - f_{t}\|_{\infty}}{\|f_{e}\|_{\infty}},$$
(23)

where f_t is the numerical solution using the time step dt. Fig. 3 shows that we observe second-order spatial (a) and temporal (b) accuracy for \mathbf{u} , T, and c. The solver satisfied incompressibility $(\nabla \cdot \mathbf{u} = 0)$ to machine precision.

3.2. Application of outlet conditions

The implementation of outlet conditions are not always fully detailed in literature. We find studies often discretize convective conditions explicitly as

$$\frac{f^{n+1} - f^n}{dt} + U_{in} \frac{\partial f^n}{\partial x} = 0, \tag{24}$$

where $\partial f/\partial x$ is approximated using first-order upwinding to add stabilizing diffusion. Though this produces an explicit f^{n+1} that can be applied as a Dirichlet condition, the resulting outlet velocity does not conserve mass. This is addressed by rescaling the outlet velocity at each time step to ensure the outlet mass flow rates balances that entering the system. This simple approach is unfortunately not always possible for membrane processes, because the mass flow rate through the membrane may not be known until after the Navier-Stokes equation has been solved, as in reverse osmosis systems [36]. We consequently investigate whether we can apply the outlet conditions implicitly as

$$\frac{\partial f^{n+1}}{\partial x} = 0, \quad \frac{f^{n+1} - f^n}{dt} + U_{in} \frac{\partial f^{n+1}}{\partial x} = 0, \tag{25}$$

to automatically satisfy mass conservation.

We present two approaches of applying conditions (25). For that purpose, Fig. 4(a) shows an outlet boundary at x=L. To simplify our presentation, we assume a uniform grid, and express the outlet velocity conditions as $a\mathbf{u}^{n+1} + b(\partial \mathbf{u}^{n+1}/\partial x) = g$, where b=1 and a=g=0 for the Neumann condition, and a=1/dt, $b=U_{in}$, and $g=\mathbf{u}^n/dt$ for the convective condition. These are discretized spatially as

$$au_e + b\left(\frac{u_e - u_w}{dx}\right) = g, \quad a\left(\frac{v_e + v_w}{2}\right) + b\left(\frac{v_e - v_w}{dx}\right) = g,$$
 (26)

where the subscripts denote the locations labeled in Fig. 4(a).

Our first method applies the discrete Eq. (26) to \mathbf{u}^* , and then modifies the outlet condition for ϕ to ensure u^{n+1} also satisfies Eq. (26) exactly. We derive the required condition for ϕ in an analogous manner to the Neumann condition (18) in Section 3.1. We begin with equation (15), repeated below

$$\mathbf{u}^{n+1} = \mathbf{u}^* - \frac{dt}{\rho} \nabla \phi. \tag{27}$$

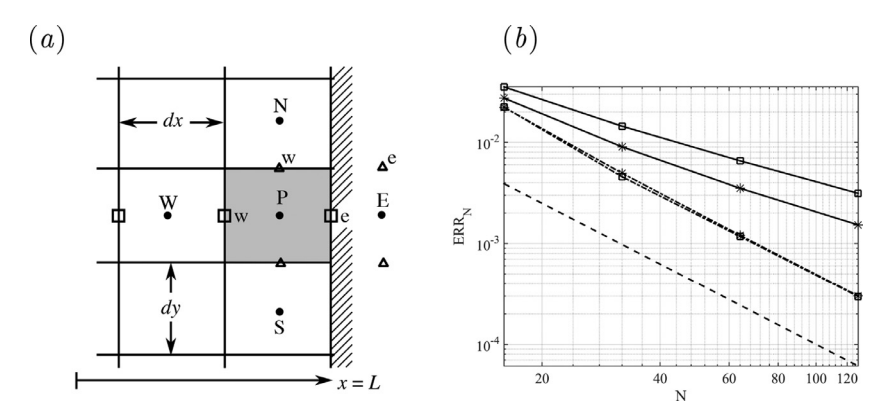


Fig. 4. (a) Sketch of the staggered grid near an outlet boundary. (b) Spatial accuracy of u (squares) and v (asterisks) when the outlet condition for ϕ enforces u^{n+1} (solid lines) or the outlet pressure (dash-dotted lines). The dashed line shows $1/N^2$.

When deriving the Poisson Eq. (16) for ϕ , we take the divergence of Eq. (27). This requires

$$\frac{\partial u^{n+1}}{\partial x} = \frac{\partial u^*}{\partial x} - \frac{dt}{\rho} \frac{\partial^2 \phi}{\partial x^2}.$$
 (28)

We now make the usual assumption that when a solving a partial differential equation subject to boundary conditions, the differential equation and conditions are both satisfied at the boundary. This suggests we can combine Eqs. (27) and (28) to express $a\mathbf{u}^{n+1} + b(\partial \mathbf{u}^{n+1}/\partial x) = g$ as

$$a\frac{\partial \phi}{\partial x}\bigg|_{x=L} + b\frac{\partial^2 \phi}{\partial x^2}\bigg|_{x=L} = \frac{\rho}{dt}\bigg[g - au^* - b\frac{\partial u^*}{\partial x}\bigg]_{x=L}.$$
 (29)

If we apply the desired outlet condition to u^* , this simplifies to

$$a\frac{\partial\phi}{\partial x}\bigg|_{x=I} + b\frac{\partial^2\phi}{\partial x^2}\bigg|_{x=I} = 0.$$
 (30)

For b = 0, this recovers the usual Neumann condition (18) from Section 3.1. Repeating the derivation on a discrete level, one finds

$$a\left(\frac{\phi_E - \phi_P}{dx}\right) + b\left(\frac{\phi_W - 2\phi_P + \phi_E}{dx^2}\right) = 0.$$
 (31)

Though condition (30) appears consistent with the underlying differential equations, one wonders if it is well-posed, as it contains a second-derivative in x. To address this issue, consider the case a=0 and b=1, for which $\partial u^{n+1}/\partial x=0$ and $\partial \phi^2/\partial x^2=0$ on the outlet. To be well-posed, this requires

$$\left. \frac{\partial^2 \phi}{\partial y^2} \right|_{x=L} = \frac{\rho}{dt} \left[\nabla \cdot \mathbf{u}^* \right]_{x=L},\tag{32}$$

which is equivalent to the Dirichlet condition

$$\phi \big|_{x=I} = \phi_L(y), \tag{33}$$

where $\phi_L(y)$ satisfies the ordinary differential equation,

$$\frac{d^2\phi_L}{dv^2} = \frac{\rho}{dt} \left[\nabla \cdot \mathbf{u}^* \right]_{x=L}. \tag{34}$$

We have found that one can indeed solve Eq. (34) numerically at each time step to apply the outlet condition $\partial^2 \phi / \partial x^2 = 0$ as an equivalent Dirichlet condition. Either method produces the same answer, and satisfies incompressibility.

The above analysis suggests we could also apply conditions (25) by applying the desired outlet conditions to \mathbf{u}^* , and then fix the outlet pressure to some desired $p_{out}(y)$ using the Dirichlet condition

$$\phi \big|_{\mathbf{y}=I} = p_{out}(\mathbf{y}) - p^n \big|_{\mathbf{y}=I}. \tag{35}$$

which is easily discretized as

$$\frac{\phi_P + \phi_E}{2} = p_{out}(y) - \frac{3p_P^n - p_W^n}{2}.$$
 (36)

Note that we must extrapolate p^n from interior nodes, because on staggered grids, the pressure at the ghost nodes is unphysical [33]. With the above approach, u^{n+1} satisfies the desired outlet condition to within a small deviation comparable to that already observed for v^{n+1} . The Poisson equation nevertheless ensures global mass conservation.

In summary, both approaches apply the desired outlet conditions (25) to \mathbf{u}^* , but differ in their treatment of ϕ . The first applies condition (30) to enforce the outlet condition for u^{n+1} exactly. The second applies the simple Dirichlet condition (35) to apply an outlet pressure. To compare the results, we first apply them to the manufactured solution

$$u_e = \sin(x)\cos(y), \quad v_e = -\cos(x)\sin(y), \quad p_e = \sin(x)\sin(y).$$
 (37)

Fig. 4(b) shows the spatial accuracy of both approaches when we solve the Navier-Stokes equations on the domain $0 \le x \le 2\pi$, $0 \le y \le 2\pi$. The outlet conditions are applied at $x = 2\pi$, with Dirichlet velocity conditions applied on all other boundaries. The solid lines show results for u (squares) and v (asterisks) when we enforce u^{n+1} . The dash-dotted lines show results using the pressure condition. Surprisingly, the latter produces second-order accuracy, while enforcing u^{n+1} produces accuracy closer to first-order. Though not shown, we found the accuracy of the first approach can be brought to second-order using a formally second-order accurate, one-sided, discretization of $\partial u/\partial x$ at the boundary. Typically, however, the actual spatial and temporal accuracy of outlet conditions is of little concern in the literature.

We next apply our outlet conditions to the simulation of flow perturbations in a planar channel flow with impermeable walls. We first perform a simulation with a fully-developed laminar velocity profile at the inlet, and the desired condition at the outlet. For cases where we fixed the outlet pressure, we set $p_{out} = 0$. The simulation is run to steady-state and the resulting flow fields, denoted $[\mathbf{U}, P]$, are used as the initial condition for a second simulation with a disturbance $v_p(y, t)$ introduced to the wall-normal inlet velocity.

$$v_p(y,t) = 0.1U_{in} \sin\left(\frac{2\pi y}{h}\right) \exp\left[-10^7 (t - .002)^2\right].$$
 (38)

This produces a perturbation near t=0.002, with a peak amplitude of $0.1U_{in}$. We run the simulation sufficiently long to allow the perturbation to interact with the outlet, and we plot the evolution of the perturbation velocity $\hat{\bf u}={\bf u}-{\bf U}$.

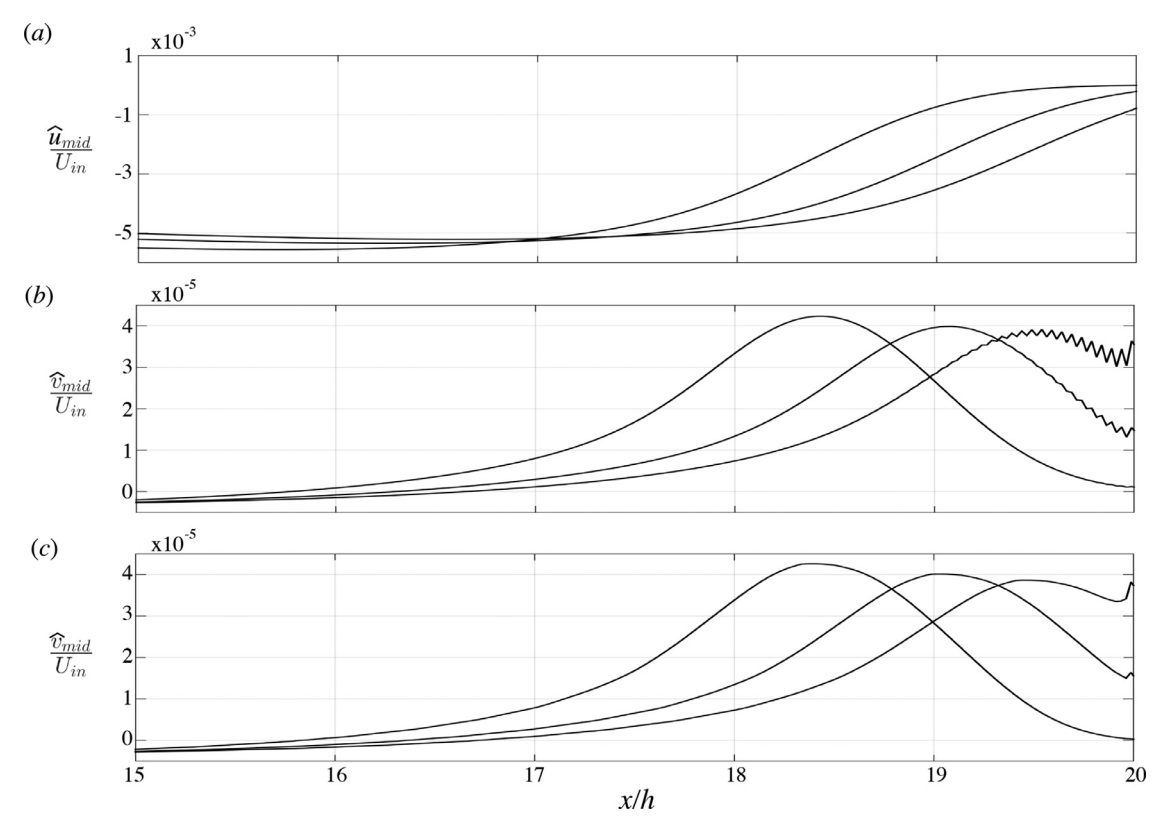


Fig. 5. Three successive snapshots of the perturbation velocity at mid-gap in a channel of aspect ratio L/h = 20 and Re = 3000. (a) Results for \widehat{u}_{mid} without a TVD scheme. (b) Results for \widehat{v}_{mid} without a TVD scheme. (c) Results for \widehat{v}_{mid} without a TVD scheme.

Fig. 5 shows results for a channel flow of aspect ratio L/h =20 and Reynolds number $Re = U_{in}h/\nu = 3000$ using the convective outlet condition. The condition for ϕ enforces the outlet value of u^{n+1} exactly. Panels (a) and (b) show three snapshots of the perturbation velocity components at mid-gap, $\hat{u}_{mid} = u(x, 0.5h, t)$ and $\widehat{v}_{mid} = v(x, 0.5h, t)$, respectively. Though the results for \widehat{u}_{mid} are smooth, \hat{v}_{mid} has unphysical oscillations on the order of $10^{-5}U_{in}$ that originate at the outlet. Such noise has been observed previously by Pauley [37] for both Neumann and convective conditions. Though likely often ignored, we prefer to attenuate outlet noise by discretizing all advection terms with a second-order TVD scheme described in Appendix B. Panel (c) shows that this removes the oscillations, and exposes rapid variations in the two cells upstream of the outlet. These are likely what triggered the oscillations in panel (b). Overall, our tests showed that both Neumann and convective conditions performed equally well, using either outlet condition for ϕ . Further investigation of our outlet conditions for cases of vortex shedding is presented in Appendix D. Due to the chronological order in which our outlet conditions for ϕ were developed, the remaining simulations in our study apply the method that enforces u^{n+1} at the outlet exactly.

To inhibit the spreading of outlet noise between adjacent channels, further testing motivated us to append "buffer cells" at the inlet and outlet of both channels. The membrane permeability and thermal conductivity are set to zero in the buffers, as sketched in Fig. 6. All other governing equations are simulated within the buffer, exactly as they are for internal cells. We found a buffer length of only two cells sufficed. When presenting simulation results, we only plot results from $0 \le x \le L$. For plotting purposes, we determine outlet values of T and c using quadratic extrapolation from upstream data. In Fig. 6, the temperature at the point marked as an open circle would be determined using T_1 , T_2 , and T_3 .

3.3. Application to polarization phenomena

We demonstrate our projection and outlet methods by simulating steady-state polarization in a bench-scale DCMD system without spacers. We set the channel dimensions to h=2 mm and L=10 cm, the inlet temperatures to $T_{in}^f=80$ °C and $T_{in}^d=20$ °C, and the inlet feed concentration to 100 g/L. The inlet velocities of both channels are set to $U_{in}=0.127$ m/s, producing the feed Reynolds number $Re_f=U_{in}h/\nu_f=600$, and the distillate Reynolds number $Re_d=U_{in}h/\nu_d=252$, where ν_f and ν_d are the feed and distillate kinematic viscosities, respectively. The membrane properties $(k_m/\delta=577 \text{ W/m}^2 \text{ K} \text{ and } B=1.87\times 10^{-6} \text{ kg/m}^2 \text{ s} \text{ Pa})$ were determined experimentally by Lou et al. [4]. The thermophysical properties of the feed and distillate are set using correlations in Lou et al. [4]. Details of the grid and mesh-independence studies are provided in Appendix C. The simulations are initiated using the inlet conditions and integrated to steady state using the Neumann outlet condition.

Fig. 7(a) shows the resulting steady-state temperature field. Different color scales are used for the feed and distillate channels to highlight the cooling of the feed and the heating of the distillate. Fig. 7(b) shows the streamwise variation of the membrane surface temperatures in the feed (T_m^f) and distillate (T_m^d) . We observe that T_m^f decreases monotonically from 80 to 47.6 °C in its downstream direction (rightwards), while T_m^d increases monotonically from 20 to 60.7 °C in its downstream direction (leftward). Fig. 7(c) shows that the temperature difference across the membrane, $\Delta T_m = T_m^f - T_m^d$, varies non-monotonically from 19.3 °C at x = 0, to a minimum of 11 °C at x/L = 6.8, and a maximum of 27.6 °C at x/L = 50.

Fig. 7 (*d*) shows the variation of the transmembrane feed velocity, $\nu_m = j_{\nu}/\rho^f$, normalized with U_{in} . We observe that though ΔT_m is maximized at the outlet, ν_m is maximized at the inlet. This

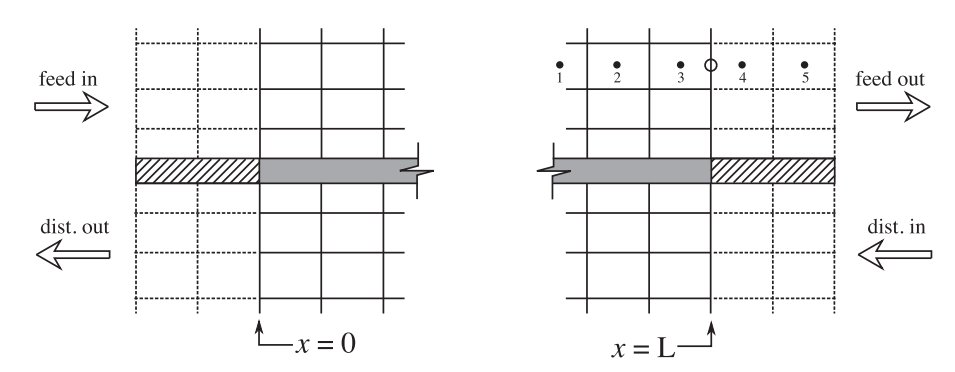


Fig. 6. Sketch of the inlet and outlet buffer cells. The membrane is shaded grey and the buffer cells are indicated using dashed lines. The membrane permeability and thermal conductivity are set to zero in the buffers.

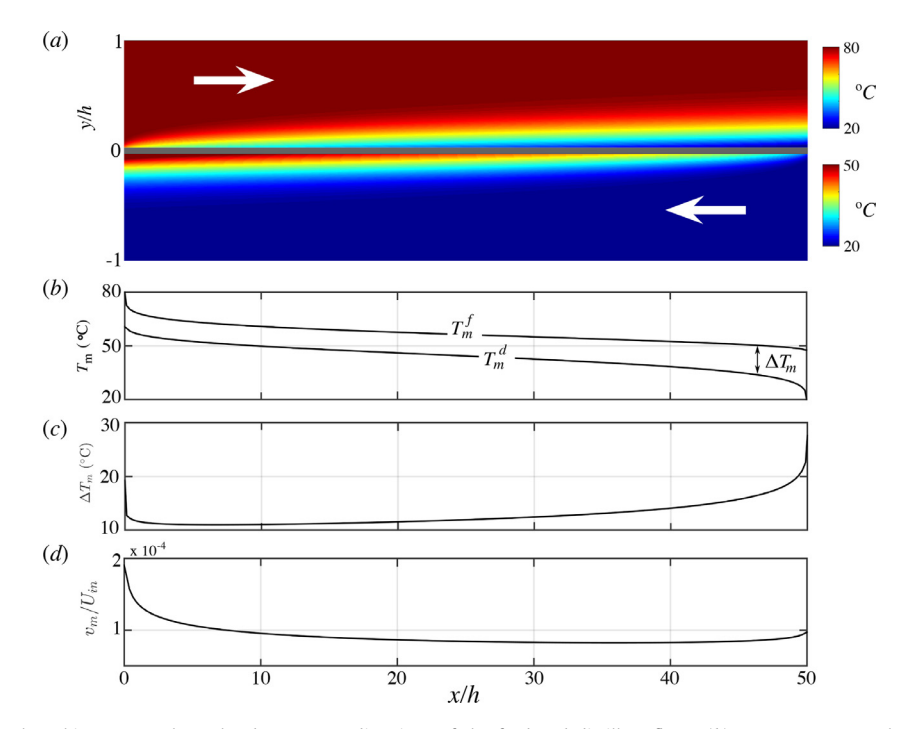


Fig. 7. (a) Temperature field. The white arrows show the downstream directions of the feed and distillate flows. (b) Temperatures on the feed and distillate membrane surfaces. (c) Transmembrane temperature difference ΔT_m . (d) Non-dimensional transmembrane velocity, v_m/U_{in} .

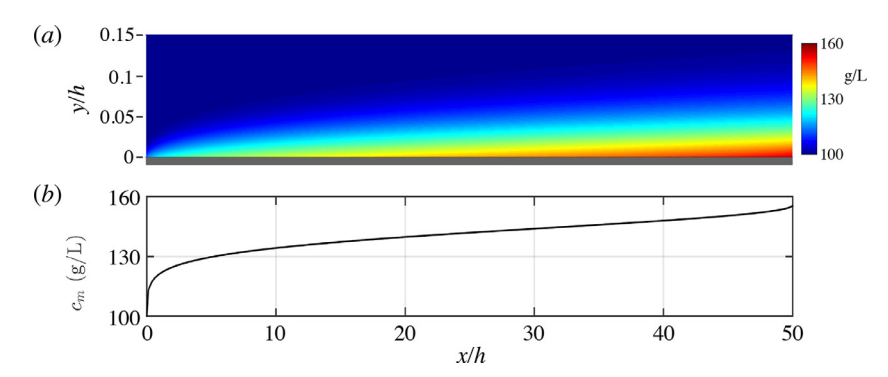


Fig. 8. (a) Concentration field for 0 < y/h < 0.15. (b) Concentration on the membrane, c_m .

occurs for two reasons. First, the saturation pressure P_{sat} varies non-linearly with temperature, such that dP_{sat}/dT increases with temperature, see Eq. (10). Second, concentration polarization is strongest at the feed outlet, where it decreases the partial vapor pressure. This is demonstrated in Fig. 8(a), which shows the feed channel concentration field. Because the mass diffusivity \mathcal{D} is much smaller than the thermal diffusivity α , the concentration

boundary layer is much thinner than the thermal layer. Consequently, Fig. 8(a) is cropped at 0 < y/h < 0.15. Fig. 8(b) shows that the membrane surface concentration, $c_m(x)$, increases significantly from 100 g/L at the inlet to 155.4 g/L at the outlet.

Fig. 9(a) shows cross-sectional temperature profiles in the feed channel at x = L/4, L/2, 3L/4, and L. To measure the downstream growth of the thermal boundary layer, we define the non-

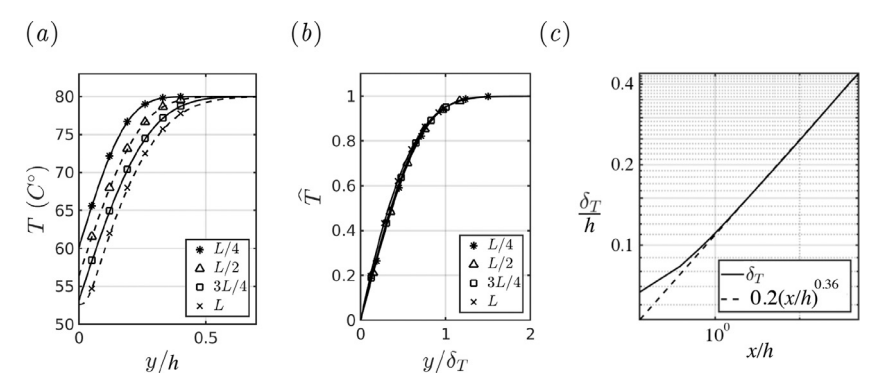


Fig. 9. (a) Temperature profiles in the feed channel at x = L/4 (asterisks), x = L/2 (triangles), x = 3L/4 (squares), and x = L (crosses). (b) Self-similar temperature distributions. (c) Numerical result (solid line) for $\hat{\delta}_T$ vs. \hat{x} . the dashed line shows the power law $\hat{\delta}_T = 0.2\hat{x}^{0.36}$.

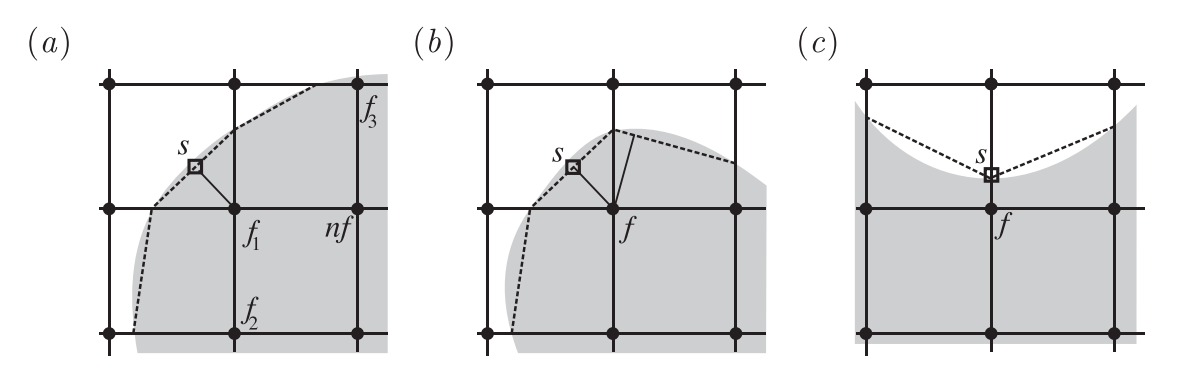


Fig. 10. Selection of forcing point and normal point. Solid regions are shaded grey. See discussion in text.

dimensional temperature

$$\widehat{T}(x,y) = \frac{T(x,y) - T_m^f(x)}{T_{in}^f - T_m^f(x)},$$
(39)

so that \widehat{T} varies from zero on the membrane to unity when $T=T_{in}^f$. We then define the boundary layer thickness δ_T as the location where

$$\widehat{T}\big|_{y=\delta_T} = 0.95. \tag{40}$$

Fig. 9(b) shows that the four curves in Fig. 9(a) collapse to a self-similar curve when \widehat{T} is plotted with the similarity variable $\eta = y/\delta_T$. Panel (c) shows that outside of the near-inlet region, δ_T grows with x as the power law $\delta_T/h = 0.2(x/h)^{0.36}$. The exponent is close to 1/3, which often occurs in thermal boundary layers due to an approximate balance between downstream advection and transverse diffusion [see discussion in Probstein 38]. Though not shown here, the concentration layer satisfies a similar power law. We refer to Lou et al. [4] for a detailed analysis.

4. Simulating spacer surfaces

We simulate spacer surfaces using a direct forcing method that extends work by Fadlun [39] and others [40–45] to simulate Neumann conditions for the temperature and concentration fields to second-order spatial accuracy. We present the method in Section 4.1 and verify its accuracy in Section 4.2 by reproducing manufactured solutions and theoretical results for the linear stability of flow over a cylinder in a plane channel. We also stress here that during the preparation of the current manuscript, a similar approach was independently reported by Yousefzadeh and Battiato [46], to whom we defer credit.

4.1. Immersed boundary method

To demonstrate our procedure, Fig. 10(a) shows nine temperature grid points (solid circles) through which six grid lines are drawn. We begin by identifying all grid points in the solid (shaded grey) for which an adjacent point on the same grid line is in the fluid. These points, called "forcing points," are labeled f_1 , f_2 , and f_3 in Fig. 10(a). The point labeled nf is not a forcing point. Though it has a neighboring point in the fluid, the two points lie on different lines. Treating such points as forcing points does not improve accuracy.

For each forcing point, we compute the shortest normal distance to the surface using a procedure similar to Majumdar et al. [40], though we use the approach of Qin et al. [47] that leverages the properties of signed distance functions. We refer to them for details, and only summarize the procedure here. Consider the point f_1 in Fig. 10(a). In the four boxes surrounding f_1 , we approximate the surface as dashed line segments joining points where the surface intersects grid lines, and then find the surface point s (square symbol) that produces the normal distance to f_1 . If multiple normal distances exist, as in Fig. 10(b), we choose the shortest. In cases where no normals exist, the surface point is set to the closest point, as in Fig. 10(c).

Our application of Dirichlet conditions is similar to that of Pacheco-Vega et al. [42]. Suppose we wish to prescribe the temperature T_s at the surface point s in Fig. 11(a). Though s does not lie on the grid, the temperature there can be approximated to second order using a bi-linear interpolation with the points labeled 1, 2, 3, and f,

$$T_s = a_f T_f + a_1 T_1 + a_2 T_2 + a_3 T_3 + \mathcal{O}(d^2), \tag{41}$$

where d is the distance between f and s, and a_f , a_1 , a_2 , a_3 are coefficients of the interpolation. From this interpolation, we can solve

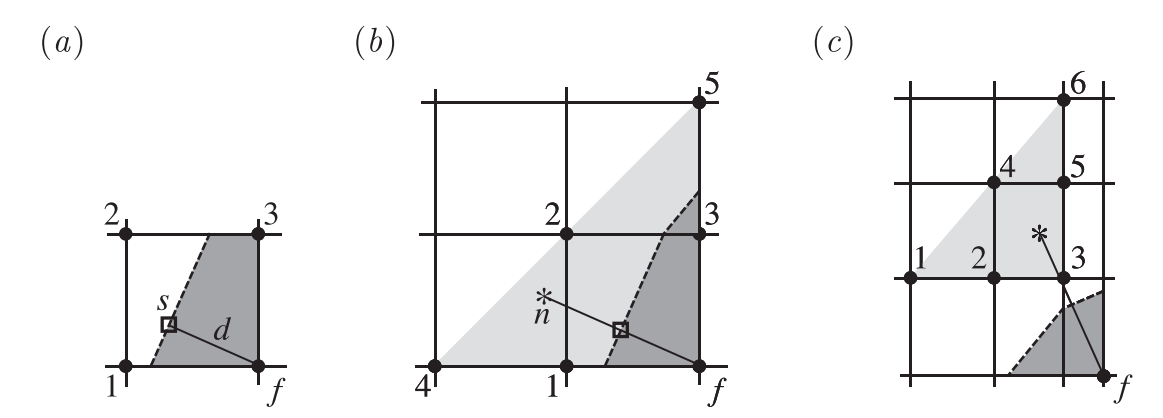


Fig. 11. Application of (a) Dirichlet and (b) Neumann boundary conditions. The triangular regions shaded light grey in panels (b) and (c) denote the interpolation space.

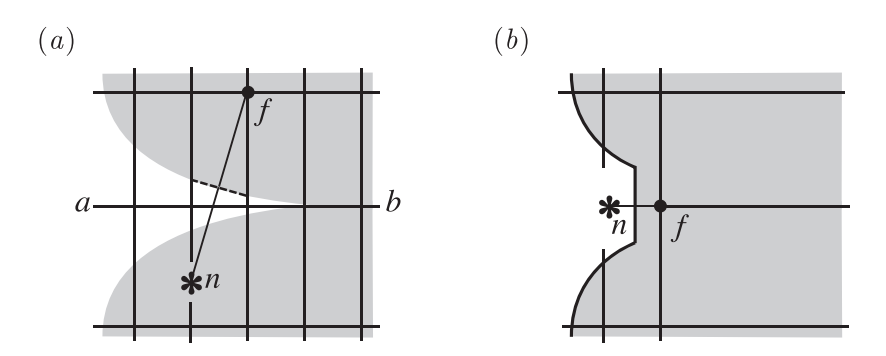


Fig. 12. At locations where an immersed surface intersects an external boundary or cusp, as in panel (a), the surface is modified as in panel (b).

for the temperature T_f

$$T_f = \frac{Ts - a_1 T_1 - a_2 T_2 - a_3 T_3}{a_f},\tag{42}$$

that must be applied at point f to satisfy the boundary condition to second-order spatial accuracy.

Next, suppose we wish to apply the Neumann condition

$$\mathbf{n} \cdot \nabla T = g_{s},\tag{43}$$

at point s in Fig. 11(b). For that purpose, we introduce the fictitious point labeled n such that s is mid-distance between points n and f. We can then discretize the boundary condition using a centered difference,

$$\frac{T_n - T_f}{2d} = g_s + \mathcal{O}(d^2). \tag{44}$$

If we approximate T_n using a bilinear interpolation, as in Eq. (41), the accuracy of the Neumann condition will be only first-order. The decreased accuracy is straightforward to show using a Taylor series, and occurs because bilinear interpolation produces a second-order spatial error in the numerator of Eq. (44). This is then divided by the denominator 2d, which is the same order as dx and dy. To obtain second-order accuracy, we approximate T_n to third order accuracy using the interpolation

$$T_n = b_f T_f + b_1 T_1 + b_2 T_2 + b_3 T_3 + b_4 T_4 + b_5 T_5 + \mathcal{O}(d^3), \tag{45}$$

where b_f and b_i ($i=1,\ldots,5$) are interpolation coefficients. Using interpolation (45) with the centered difference (44) produces net second-order accuracy.

For the case sketched in Fig. 11(b), the fictitious point n lies in the triangular interpolation space shaded light grey. When the point lies outside this space, we interpolate as demonstrated in Fig. 11(c) to avoid extrapolation. Another special case occurs when an immersed surface has a cusp, as in Fig. 12(a). Cusps are also

generated when an immersed surface intersects the external domain of the simulation. This would occur in Fig. 12(a) if the line labeled ab was the external boundary. Such cusps project the point n back into the solid or outside the domain. Refining the grid tends to simply push the issue further into the cusp. We address this issue as suggested by Finn and Apte [48], by locally modifying the immersed surface as in Fig. 12(b).

As earlier mentioned, our approach is similar to that of Youse-fzadeh and Battiato [46]. There are some differences worth mentioning. We integrate the pressure field using a projection method, while Yousefzadeh and Battiato use the SIMPLE scheme [49]. Our grids are non-uniform, while those of Yousefzadeh and Battiato are uniform. While we focus on immersed Neumann and Dirichlet conditions, Yousefzadeh and Battiato consider more general immersed Robin conditions. Next, while we reconstruct the immersed surface using the distance function method of Qin et al. [47], Yousefzadeh and Battiato use a ray-casting method. Finally, in contrast to our interpolation stencils sketched in Fig. 11, Yousefzadeh and Battiato propose stencils that exclude the forcing point to increase the stability and convergence of their iterative SIM-PLE scheme. In our case, we have not observed any stability issues

4.2. Verification and validation

We verify the spatial and temporal accuracy of our direct forcing method using the forced analytical solution

$$\begin{bmatrix} u_e \\ v_e \\ p_e \\ T_e \end{bmatrix} = \begin{bmatrix} \sin(x)\cos(y) \\ -\cos(x)\sin(y) \\ \sin(x)\sin(y) \\ \sin(x)\sin(y) \end{bmatrix} \cos(\omega t). \tag{46}$$

We set all thermophysical properties to unity, and solve the continuity, Navier-Stokes, and heat Eqs. (1) and (2) in the do-

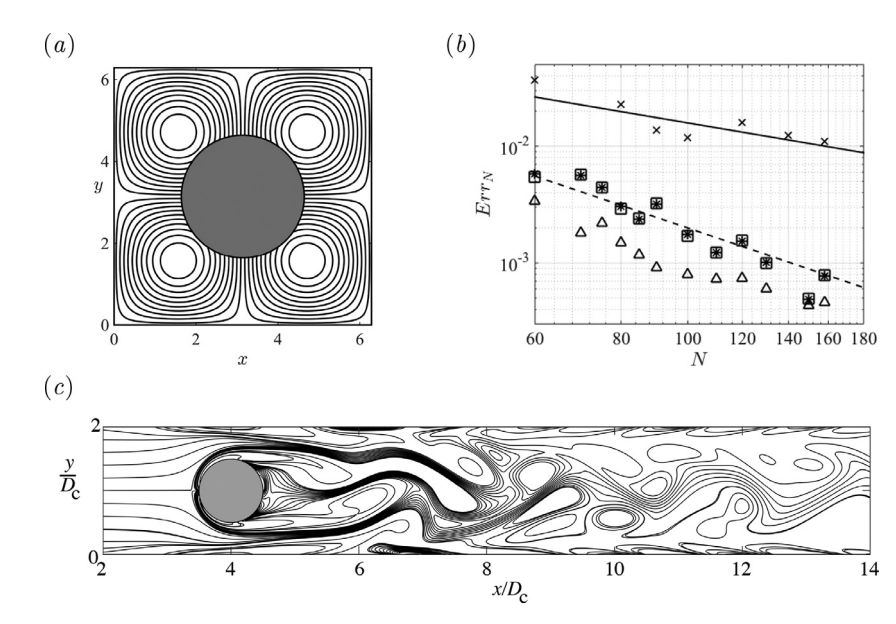


Fig. 13. (a) Streamlines of the test solution. (b) Err_N vs. N for u (squares), v (asterisks), and T (triangles) using the third-order interpolation for the Neumann condition. The crosses show Err_N for T when the bi-linear interpolation is used for the Neumann condition. The dashed and dash-dotted lines show slopes of $1/N^2$ and 1/N, respectively. (c) Instantaneous vorticity contours in a channel with an immersed cylinder when $(Re, \beta) = (266.7, 0.5)$. This case is equivalent to that in Fig. 11 of Sahin and Owens [20].

main $(x, y) \in [0, 2\pi] \times [0, 2\pi]$ with a circular cylinder of diameter $D_c = 3$ centered at $(x,y) = (\pi,\pi)$, as illustrated in Fig. 13(a). On the cylinder surface, we apply the Dirichlet condition $\mathbf{u} = \mathbf{u}_e$, and the Neumann condition $\mathbf{n} \cdot \nabla T = \mathbf{n} \cdot \nabla T_e$. On the external boundaries, we apply Dirichlet conditions to \mathbf{u} and T. As in Section 3.1, we test the spatial accuracy by setting $\omega = 0$ and integrating to steady-state from the initial condition $\mathbf{u} = p = T = 0$. Simulations were performed using a non-uniform grid with Gauss-Lobatto-Chebyshev distributions in the x and y-directions.

Fig. 13(b) shows that our method produces second-order spatial accuracy for the velocity and temperature fields when using the third-order interpolation for the Neumann condition. The scatter arises due to the nonlinear distribution of the grid points. Repeating the analysis with a uniform grid produces much smoother results. The cross symbols show that using a bi-linear interpolation for the Neumann condition reduces the accuracy of *T* to first-order. Though not shown for brevity, we also confirmed second-order temporal accuracy, and repeated our analysis for several cylinder locations.

We validate our ability to simulate vortex shedding by comparing to a linear stability analysis performed by Sahin and Owens [20] of fully-developed channel flow with a circular cylinder on the centerline. We place the cylinder at least 3 diameters from the inlet and at least seven diameters from the outlet. We define the blockage ratio $\beta = D_c/h$ and Reynolds number $Re = U_{in}h/\nu$. To compute the critical Reynolds number for transition to vortex shedding, we perform simulations to determine two Reynolds numbers Re_1 and Re_2 , for which $Re_2 - Re_1 \le 5$ and for which the flow is steady at Re1 and unsteady at Re2. The critical Reynolds number is then set to $Re_c = (Re_1 + Re_2)/2$. At the unsteady Reynolds number Re2, we compute the dominant frequency f_c of oscillation by recording the centerline velocity at a location downstream of the cylinder. We define the critical Strouhal number as $St_c = f_c D_c / U_{in}$. Table 1 demonstrates excellent agreement between our results and those of Sahin and Owens [20]. As further validation, Fig. 13(c) shows instantaneous vorticity contours when $(Re, \beta) = (266.7, 0.5)$. These show excellent agreement with those shown in an identical simulation reported in Fig. 11 of Sahin and Owens [20].

Table 1 For the blockage ratios $\beta = D/h$ in the first column, the remaining columns compare the critical Reynolds number and Strouhal numbers computed in the current study (columns 2–3) with those of Sahin and Owens (columns 4–5).

	Current study		Sahin and Owens [20]	
β	Re _c	St	Re_c	St
0.3	$213\ \pm 2$	0.317	212	0.312
0.5	168 ± 1	0.509	167	0.505
0.7	$106\ \pm\ 0.5$	0.681	106	0.707

5. Application to unsteady transport in DCMD systems

We now use our methods to simulate polarization in a DCMD system with spacers. We consider a short system of dimensions h=2 mm and L=20 mm with cylinders of diameter $D_{\rm C}=1$ mm placed on the centerlines of both channels at x=10 mm. The length ensures the spacers are a distance of 10 diameters from the inlet and outlet. As in Section 3.3, we set the operating temperatures to $T_{in}^f=80~{}^{\circ}{\rm C}$ and $T_{in}^d=20~{}^{\circ}{\rm C}$, and the feed concentration to $C_{in}=100~{\rm g/L}$. The simulations are run to steady state for subcritical cases, and run sufficiently long to attenuate any transient startup effect for supercritical cases. Simulations were repeated using both Neumann and convective outlet conditions. The difference in the results were negligible.

Fig. 14 shows results when $U_{in}=2.11\times 10^{-2}$ m/s. This produces the Reynolds numbers $Re_f=100$ and $Re_d=42$, for which the flow is steady in both channels. The streamlines in panel (a) show a pair of counter-rotating vortices in the downstream wakes of each spacer. As expected, the wake is larger in the feed channel due to its larger Reynolds number. Panels (b) and (c) show that as the feed and distillate flows accelerate around the spacers, the temperature and concentration boundary layer thicknesses decrease, due to the increase in downstream advection. Because the concentration layer is quite thin, panel (c) shows results for $0 \le y/h \le 0.2$.

The solid lines in Fig. 15 show the transmembrane temperature difference ΔT_m (a), surface concentration c_m (b), and transmembrane feed velocity v_m/U_{in} (c). The dashed lines show results for a

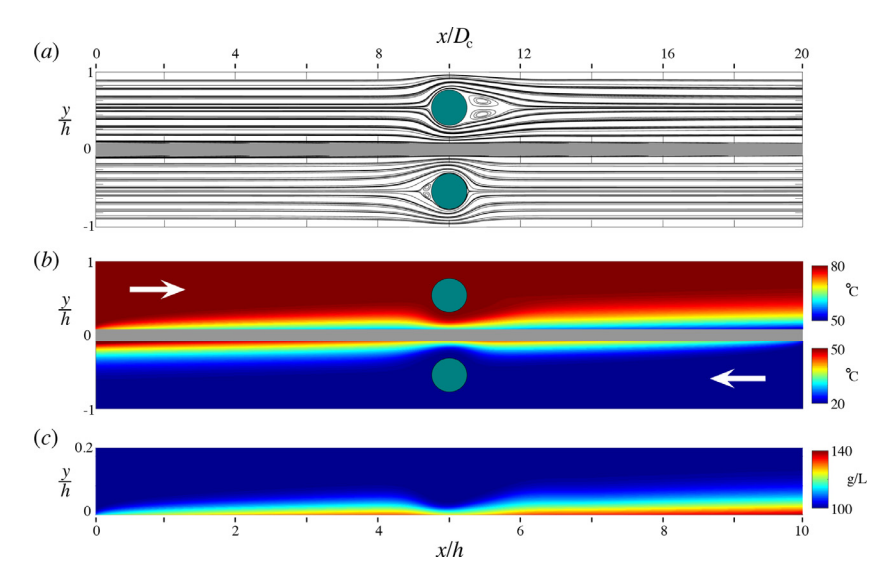


Fig. 14. (a) Steady-state streamlines, (b) temperature field, and (c) feed concentration field for the subcritical case $Re_f = 100$ and $Re_d = 42$. Different color scales are used for temperatures in the feed and distillate channels. The concentration field is shown for 0 < y/h < 0.2. For convenience, we present the position as both x/h and x/D_c .

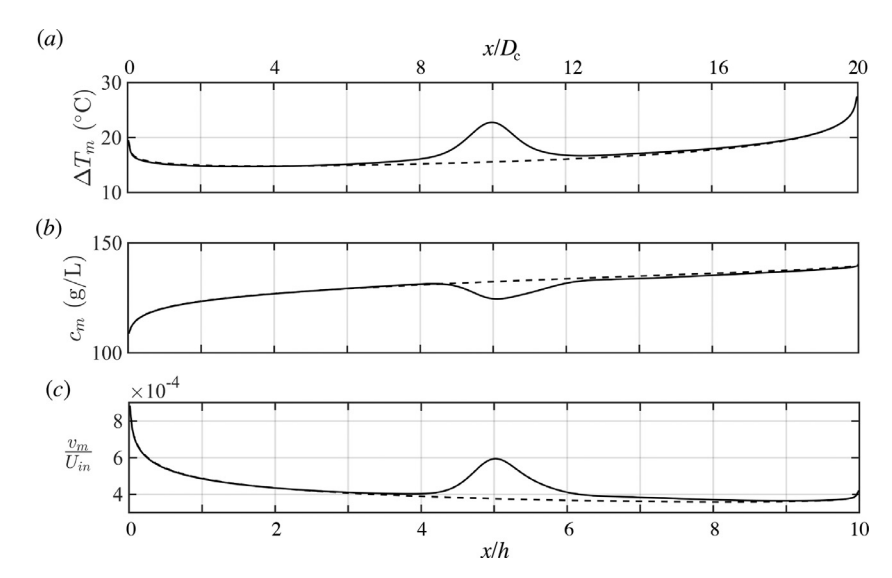


Fig. 15. Steady-state results for (a) the transmembrane temperature difference ΔT_m , (b) the membrane surface concentration c_m , and (c) the transmembrane vapor flux v_m/U_m for the subcritical case $Re_f = 100$ and $Re_d = 42$. The solid and dashed lines show results of simulations performed with and without spacers, respectively.

simulation performed without the cylinders. We see that the influence of the spacers is limited to a region extending roughly two cylinder diameters up and downstream from the cylinder center. In that region, the cylinders increase ΔT_m , decrease c_m , and increase vapor production. Overall, the simulation with the spacers produces an average transmembrane vapor flux of 9.4×10^{-6} m/s, compared to 8.5×10^{-6} m/s for the case without spacers, an increase of 10.6%.

Fig. 16 shows snapshots of the streamlines (a), temperature field (b), and concentration field (c) when we increase the inlet velocity to $U_{in}=8.46\times10^{-2}$ m/s, producing the Reynolds numbers $Re_f=267$ and $Re_d=112$. Based on $Re_c=168$ in Table 1, the distillate flow is subcritical and the feed flow is strongly supercritical ($Re_f-Re_c=99$). Note that we performed additional simulations to determine the critical Reynolds number of the fully coupled DCMD system, and found the presence of the membrane and transmembrane flow had a negligible effect on Re_c . Panel (a) shows that instability in the feed channel produces strong wake oscillations and a pair of staggered recirculation zones that periodically appear and travel downstream along the membrane and outer wall. The pe-

riod for the formation of these recirculation regions is identical to that of the vortex shedding behind the cylinder. Snapshots showing the evolution of these wall and membrane vortices are provided in Fig. 17. The temperature plot in Fig. 16(*b*) suggests that the leading edge of the recirculation zone traveling along the membrane tends to eject near-membrane cool fluid into the bulk flow. This in turn brings warmer bulk fluid towards the membrane.

The concentration plot in Fig. 16(c) shows that the recirculation zone is not similarly able to eject high concentration fluid into bulk. This is likely due to the fact that the concentration boundary layer is much thinner than the temperature layer. We also observe a local region of salt accumulation near x/h = 6.3. Closer inspection suggests that this occurs because the flow reversal within the recirculation zone advects solutes upstream along the membrane surface where they meet downstream advection of solutes at the leading edge of the recirculation zone.

The solid lines in Fig. 18 show snapshots of ΔT_m (a), c_m (b), and v_m/U_{in} (c) for the simulation with spacers. The dashed lines show the results of a simulation performed without spacers. Though the feed channel is strongly unsteady, the results at the membrane for

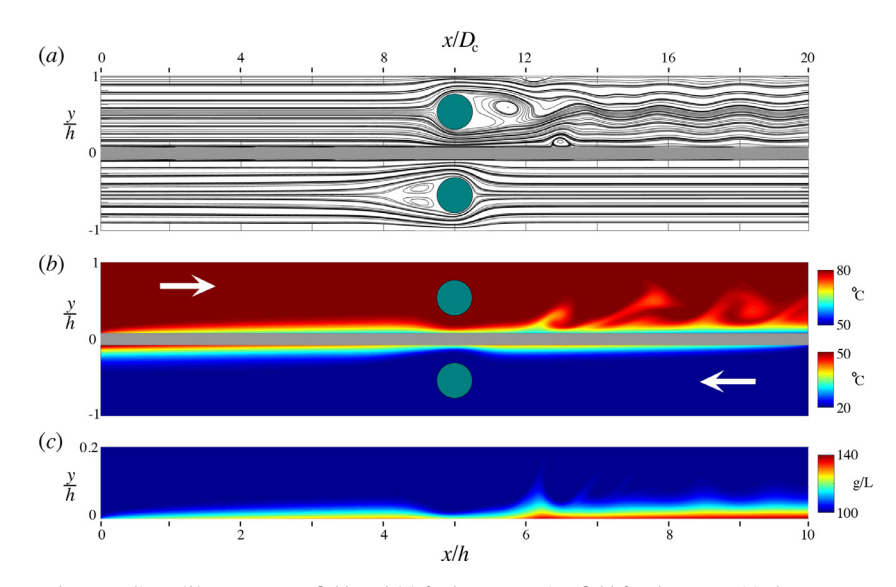


Fig. 16. Snapshots of (a) the unsteady streamlines, (b) temperature field, and (c) feed concentration field for the supercritical case $Re_f = 267$ and $Re_d = 112$. Different color scales are used for temperatures in the feed and distillate channels. The concentration field is shown for 0 < y/h < 0.2. For convenience, we present the position as both x/h and x/D_c .

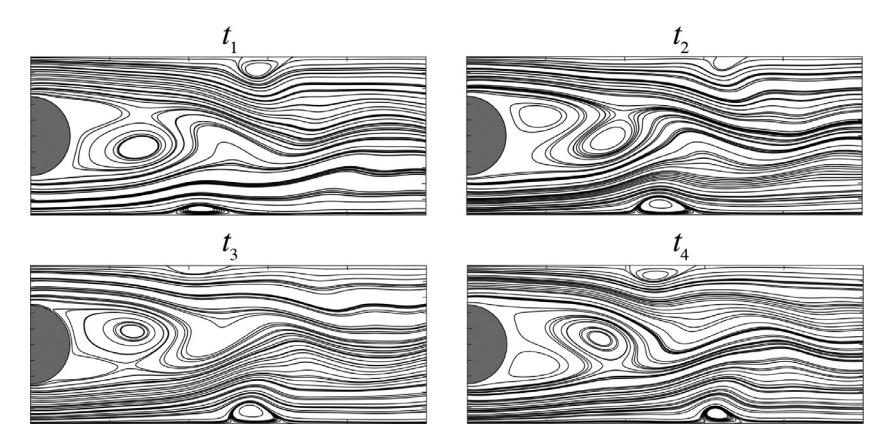


Fig. 17. Snapshots of the streamlines at four equispaced times $t_1 < t_2 < t_3 < t_4$ where $t_n - t_{n-1}$ is approximately $3/(13f_s)$, where $f_s = 34$ Hz is the shedding frequency.

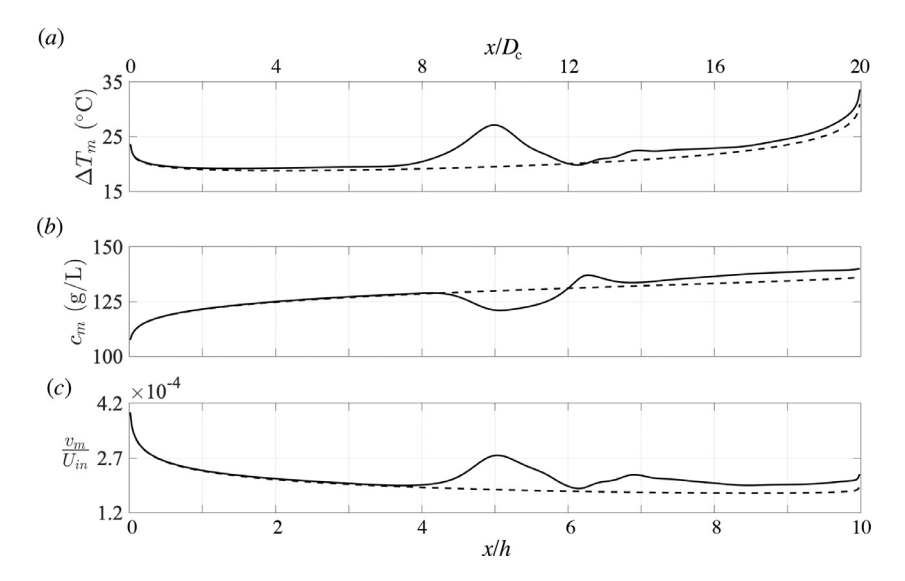


Fig. 18. The (a) transmembrane temperature difference ΔT_m , (b) membrane surface concentration c_m , and (c) transmembrane vapor flux v_m/U_{in} for the supercritical case $Re_f = 267$ and $Re_d = 112$. The solid and dashed lines show results of simulations performed with and without spacers, respectively.

 ΔT_m , c_m , and v_m are all essentially steady, showing only negligible variations in time. Panel (a) shows that the spacer increases ΔT_m , not only near the spacer, but also in the far downstream region. Panel (b) shows that while concentration polarization is reduced below the spacer, there is a region of preferential salt accumulation near x/h = 6.3. Overall, the simulation with the spacers produces an average transmembrane vapor flux of 1.25×10^{-5} m/s, compared to 1.10×10^{-5} m/s without spacers, an increase of 14.3%. Though not shown here for brevity, we found that as we further increase U_{in} , and consequently the Reynolds numbers, the spacers continue to increase vapor production over what is observed without spacers. Unfortunately, the maximum concentration within the region of preferential salt accumulation also grows significantly, suggesting that the increase in vapor production comes with a risk of increasing salt precipitation. To our knowledge, the current study is the first to report a potential tradeoff between vapor production and concentration polarization in DCMD systems. Though beyond the current scope, we can report that we have performed preliminary simulations of spacer filaments in reverse osmosis systems, and observed similar behavior. We consequently do not believe this tradeoff to be unique to membrane distillation. Finally, while we have focused here on polarization and vapor production, spacer filaments have an important impact on the downstream pressure gradients in the feed and distillate channels. For brevity, we do not report those results here, as they are the topic of a more in-depth parametric study currently underway.

6. Conclusions

In addition to DCMD's important industrial applications, the process touches on numerous long-standing issues in both theoretical and computational fluid mechanics. The numerical issues include (1) extending projection methods to more general Robin boundary conditions; (2) developing approximate outlet conditions that conserve mass in open systems with multiple inlets and outlets; and (3) simulating complex geometries in flows with heat and mass transport. The theoretical issues include (1) heat and mass boundary layers with complicated wall-interactions, as opposed to the classic case of a thermal boundary layer evolving over a wall maintained at a constant temperature or heat flux; (2) understanding transitions of flow regimes over bluff bodies; and (3) understanding how vortical flow structures influence mixing and interact with adjacent surfaces. Though not discussed here, further issues include multi-species transport in complex feed solutions, and the physics of nucleation and precipitation.

We showed that transport in the coupled feed and distillate channels can be simulated using a projection method that applies membrane boundary conditions using Adams-Bashforth extrapolation to solve the two channels sequentially, instead of simultaneously. We also showed that mass can be automatically conserved in the open system using Neumann and convective outlet conditions that are applied implicitly within a projection method. Though outside the scope of the current study, this approach is crucial for our parallel work simulating pressure-driven membrane separation processes such as reverse-osmosis. In these systems, the mass flow rate through the membrane is only known after the solution of the Poisson problem for ϕ , as discussed in Tilton et al. [36].

We also showed that Neumann conditions can be simulated to second order spatial and temporal accuracy using a direct forcing immersed boundary method. We validated the method against forced analytical solutions and theoretical predictions of a linear stability analysis of transition to vortex shedding. We again note that a similar approach was recently independently reported by Yousefzadeh and Battiato [46], to whom we defer credit. Future work should extend this method to three-dimensions. Future work

may also wish to explore whether it is better to formally apply immersed Neumann conditions to second order accuracy, as in our study, or if one can achieve comparable accuracy using a simpler first-order approach with Adaptive Mesh Refinement (AMR) at the immersed surface. Our approach requires a larger stencil at the immersed surface, and consequently reduces the sparsity of matrices required for semi-implicit temporal discretizations. This may influence memory, parallelization, and CPU time. That issue deserves a dedicate study using optimized codes. In contrast, the current study uses preliminary, un-optimized, sequential codes.

Finally, we applied our methods to simulate heat and mass transport in DCMD systems with and without an idealized two-dimensional spacer filament on the channel centerlines. We note that our results for the case without spacers were recently reported in much greater detail in a separate publication [4]. The results for cases with a spacer are the topic of an ongoing parametric study. Within the limits of the current study, we showed that in steady flow regimes, the spacer filaments had a net positive impact by decreasing both temperature and concentration polarization, and thereby increasing permeate production. In supercritical flow regimes, however, the spacers improved permeate production at the expense of generating regions of preferential solute accumulation. That increases the risk of precipitation when treating high-concentration feed solutions, which is a major application of interest for DCMD systems.

Declaration of Competing Interest

The authors declare that they have no known competing financial interests or personal relationships that could have appeared to influence the work reported in this paper.

CRediT authorship contribution statement

Jincheng Lou: Conceptualization, Methodology, Software, Writing - original draft. **Jacob Johnston:** Conceptualization, Methodology, Software, Writing - original draft. **Nils Tilton:** Supervision, Conceptualization, Methodology, Software, Writing - original draft.

Acknowledgments

This work was generously supported by the Colorado School of Mines Slater Family Research Fund, the U.S. Bureau of Reclamation (R16AC00121), the Colorado Office of Economic Development and International Trade, and a National Science Foundation CAREER Award (1752531). The authors thank Drs. Tony Saad (University of Utah), Amneet Pal Bhalla (San Diego State University), Denis Martinand (University of Aix-Marseille), and Amir Riaz (University of Maryland), for helpful discussions. We also thank Drs. Paul Martin and Greg Fasshauer (Colorado School of Mines) who suggested our derivation of the outlet ϕ conditions in Section.

Appendix A. Transmembrane heat transport

Here we provide a brief derivation of the Schofield model [25] of heat transport through MD membranes. Instead of simply repeating the original derivation, we provide an alternate approach that highlights heat transport at the liquid-vapor interfaces. Fig. 19(a) depicts an idealized membrane whose surface is the plane y=0. Liquid occupies the region y>0. The membrane, composed of a solid phase and vapor-filled pores, occupies the region y<0. To simplify our analysis, we neglect surface tension and assume all liquid-vapor and liquid-solid interfaces lie in the plane y=0, as in Fig. 19(a). More detailed discussion of surface tension effects can be found in the work of Lawson and Lloyd [50]. We assume the liquid-solid and liquid-vapor interfaces are in thermal

equilibrium, such that the temperature is continuous at y=0. The temperature gradient $\partial T/\partial y$ is generally discontinuous. For discussion of these common assumptions, we refer to the classic works of Leal [29] and Prosperetti [51]. In the following, we consider heat transport across the plane y=0 on the pore-scale. This is then upscaled to produce a practical macroscopic model.

At liquid-solid interfaces, heat is transported by conduction only,

$$-k_{l} \frac{\partial T}{\partial y} \bigg|_{y=0^{+}} = -k_{s} \frac{\partial T}{\partial y} \bigg|_{y=0^{-}}$$
(47)

where k_l and k_s are the thermal conductivities of the liquid and solid, respectively. For this Appendix, the subcripts $y=0^+$ and $y=0^-$ denote the evaluation of the gradient as y approaches zero from above and below, respectively. At liquid-vapor interfaces, heat is transported by conduction and advection. Conservation of thermal energy at the liquid-vapor interfaces [29,51] requires

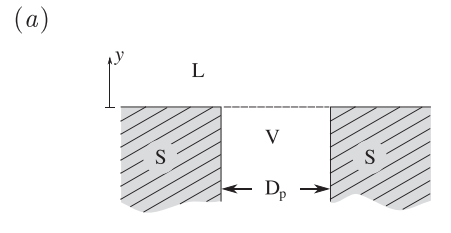
$$-k_{l} \frac{\partial T}{\partial y} \bigg|_{y=0^{+}} + \rho_{l} \nu_{l} h_{l} \bigg|_{y=0^{+}} = -k_{s} \frac{\partial T}{\partial y} \bigg|_{y=0^{-}} + \rho_{v} \nu_{v} h_{v} \bigg|_{y=0^{-}}, \tag{48}$$

where h is the enthalpy per unit mass, and the subscripts l and v distinguish between properties of the liquid and vapor, respectively. The left-hand-side of Eq. (48) represents heat conduction and advection crossing the interface from the liquid side of the interface, while the right-hand-side represents conduction and advection from the vapor side. Using conservation of mass ($\rho_l v_l = \rho_\nu v_\nu$), Eq. (48) can be rewritten as

$$-k_l \frac{\partial T}{\partial y}\Big|_{y=0^+} + k_s \frac{\partial T}{\partial y}\Big|_{y=0^-} = \rho_l \nu_l \Big(h_\nu \big|_{y=0^-} - h_l \big|_{y=0^+}\Big) = \rho_l \nu_l \lambda. \tag{49}$$

To upscale the pore-scale heat transport represented by Eqs. (47) and (49), we introduce the circular averaging area $\mathcal A$ sketched in Fig. 19(b). We assume the diameter of the averaging area is much larger than a typical pore diameter ($D_A \gg D_p$) but also much smaller than the channel height ($D_A \ll h$), which is naturally satisfied in MD systems. At every point (x, z) on the membrane surface, we define area-averaged fields of the form

$$\langle v \rangle (x, z, t) = \frac{1}{\mathcal{A}} \int_{\mathcal{A}} v \Big|_{y=0} dA, \quad \left\langle \frac{\partial T}{\partial y} \right\rangle (x, z, t) = \frac{1}{\mathcal{A}} \int_{\mathcal{A}} \left. \frac{\partial T}{\partial y} \right|_{y=0} dA.$$



To reproduce the Schofield model, we approximate the average heat transport crossing the plane y = 0 from the liquid side as

$$q_{m} = \underbrace{-(1-\phi)k_{l}\left\langle\frac{\partial T}{\partial y}\right\rangle\Big|_{0^{+}}}_{\text{liquid-solid interfaces}} \underbrace{-\phi k_{l}\left\langle\frac{\partial T}{\partial y}\right\rangle\Big|_{0^{+}}}_{\text{liquid-vapor interfaces}} + \rho_{l}\langle\nu_{l}\rangle\langle h_{l}\rangle\Big|_{0^{+}}, (51)$$

where ϕ is the area porosity of the membrane surface. The first term in Eq. (51) represents heat conduction across liquid-solid interfaces. The second and third terms represent heat conduction and advection across the liquid-vapor interfaces, respectively. The approximation (51) assumes one effective temperature gradient for both the liquid-solid and liquid-vapor interfaces. Similarly, we approximate the average heat transport crossing the plane y=0 from the membrane side as

$$q_{m} = -(1 - \phi)k_{s} \left(\frac{\partial T}{\partial y}\right)\Big|_{0^{-}} - \phi k_{\nu} \left(\frac{\partial T}{\partial y}\right)\Big|_{0^{-}} + \rho_{\nu} \langle \nu_{\nu} \rangle \langle h_{\nu} \rangle\Big|_{0^{-}}. (52)$$

Though approximations (51) and (52) are intuitive, a more formal derivation could consider the method of volume-averaging [52], which has been used extensively to model heat, mass, and momentum transport across porous surfaces [53]. Such analysis is beyond the scope of this study.

Equating expressions (51) and (52), and applying conservation of mass produces

$$-k_{l}\left(\frac{\partial T}{\partial y}\right)\Big|_{\Omega^{+}} = -k_{m}\left(\frac{\partial T}{\partial y}\right)\Big|_{\Omega^{-}} + j_{\nu}\langle\lambda\rangle,\tag{53}$$

where $k_m=(1-\phi)k_S+\phi k_{\nu}$ is the membrane thermal conductivity [25]. If we assume a linear temperature gradient within the membrane, the area-averaged temperature gradient on the membrane side of the interface $(y=0^-)$ can be approximated as $(T_m^d-T_m^f)/\delta$. Furthermore, if the averaging area is small compared to the channel $(D_A\ll h)$, the brackets can be removed from the left-hand-side of Eq. (53) and the latent heat term so that Eq. (53) becomes

$$-k_l \frac{\partial T}{\partial y}\Big|_{0^+} = -\frac{k_m}{\delta} \left(T_m^f - T_m^d \right) + j_v \lambda, \tag{54}$$

which recovers the thermal boundary condition (12).

Appendix B. Spatial discretization

(b)

Fig. 20 demonstrates our staggered grid. As sketched in panel (a), the variables p, T, and c are stored at the cell centroids, while u and v are stored at cell faces. To discretize the x-component of the Navier-Stokes equation, we consider the control volume shaded

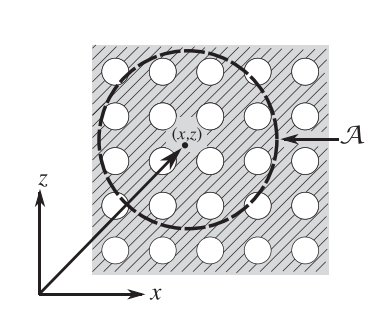


Fig. 19. (a) Idealized cross-section of a membrane pore showing the liquid (L), solid (S), and vapor (V) regions. The dashed line represents the liquid-vapor interface, in which curvature due to surface tension is neglected. (b) Sketch of the averaging area *A*.

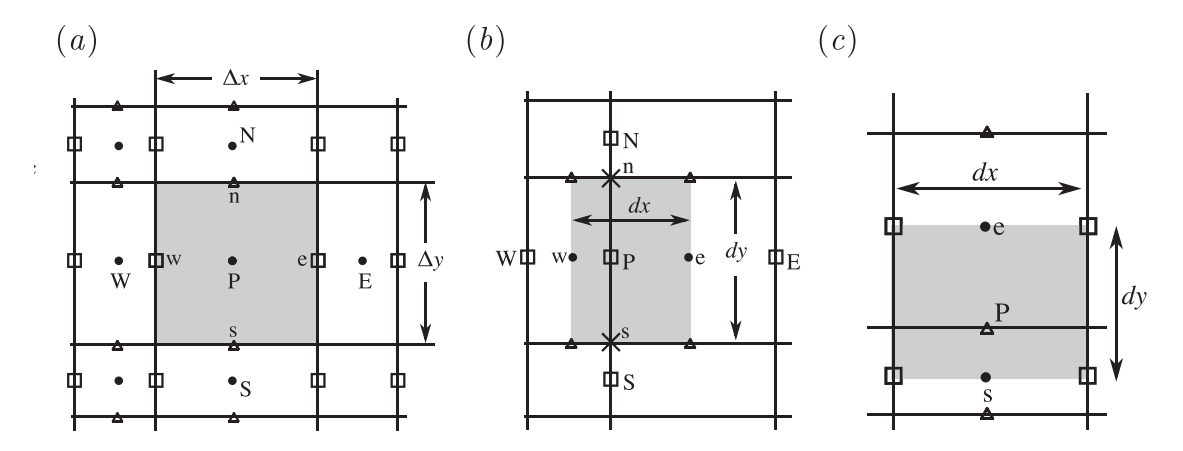


Fig. 20. The staggered grid. The fields u, v, and p are stored at the locations marked as squares, triangles, and solid dots, respectively. (a) A pressure cell (shaded grey). (b) The control volume (shaded grey) used to discretize momentum in the y-direction.

grey in Fig. 20(b). We write the equation in control volume form as

$$\int_{CV} \rho \frac{\partial u}{\partial t} dV + \int_{S} \rho u(\mathbf{u} \cdot \mathbf{n}) dA = -\int_{S} p(\mathbf{i} \cdot \mathbf{n}) dS + \int_{S} \mu (\nabla u \cdot \mathbf{n}) dA,$$
(55)

where \mathbf{i} is the unit vector in the *x*-direction, \mathbf{n} is the unit normal vector pointing away from the control surface *S* of the control volume *CV*. We approximate the volume integral and pressure term in Eq. (55) as

$$\int_{V} \rho \frac{\partial u}{\partial t} dV \approx \rho \frac{\partial u_{P}}{\partial t} dx dy, \quad \int_{S} p(\mathbf{i} \cdot \mathbf{n}) dS \approx P_{e} dy - P_{w} dy, \tag{56}$$

where dx and dy are the distances labeled in Fig. 20(b). We approximate the advection term in Eq. (55) as

$$\int_{\mathcal{S}} \rho u(\mathbf{u} \cdot \mathbf{n}) dA \approx \dot{m}_e u_e + \dot{m}_n u_n - \dot{m}_w u_w - \dot{m}_s u_s, \tag{57}$$

where $\dot{m}_e = \rho u_e dy$, $\dot{m}_n = \rho v_n dx$, $\dot{m}_w = \rho u_w dy$, and $\dot{m}_s = \rho v_s dx$ denote the mass flow rates through the four faces of the volume. The subscripts n and s denote the face locations marked with crosses in Fig. 20(b). The velocities within the mass flow rates are approximated using linear interpolation. For example, we compute the velocity within \dot{m}_n as

$$v_n \approx (1 - \alpha)v_{nw} + \alpha v_{ne}, \quad \alpha = \frac{x_n - x_{nw}}{dx}.$$
 (58)

We considered two methods of approximating the four face values of u that multiply the mass flow rates in Eq. (57). The first, commonly called "centered differencing," approximated the velocities using the same linear interpolation procedure above. The second used a TVD scheme, which improved the outlet conditions. We compared the performance of several TVD schemes, and the scheme commonly called "minmod" worked well. We refer readers to reference [54] for details. For demonstration, the scheme approximates u_{ℓ} as

$$u_e = u_e^{low} - \phi_e(r_e)(u_e^{low} - u_e^{high}),$$
 (59)

where u_e^{low} and u_e^{high} are evaluated using first-order upwinding and centered differencing, respectively, and $\phi = \max[0, \min(r, 1)]$, where r is the ratio of successive gradient in the flow direction.

Finally, we approximate the viscous term in Eq. (55) as

$$\int_{S} \mu(\nabla \mathbf{u} \cdot \mathbf{n}) dA \approx \mu \frac{\partial u_{e}}{\partial x} dy + \mu \frac{\partial u_{n}}{\partial y} dx - \mu \frac{\partial u_{w}}{\partial x} dy - \mu \frac{\partial u_{s}}{\partial y} dx, \qquad (60)$$

where the gradients are approximated using centered differences, such as

$$\frac{\partial u_e}{\partial x} \approx \frac{u_E - u_P}{x_E - x_P}. ag{61}$$

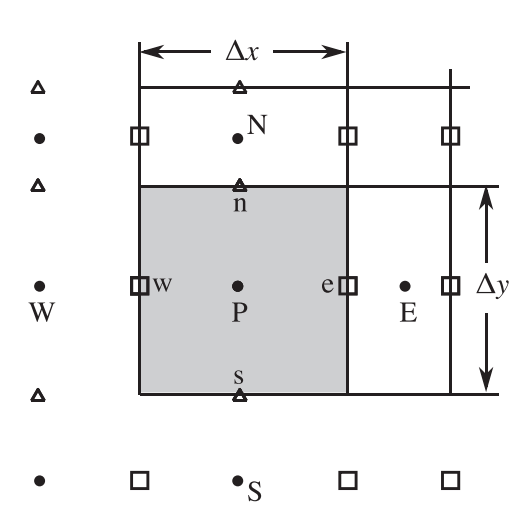


Fig. 21. A corner pressure cell (shaded grey) with ghost nodes.

The above approach is repeating to discretize the *y*-momentum equation using the control volume sketched in Fig. 20(c). We then find that Eq. (15) is expressed in discrete form as

$$u_p^{n+1} = u_p^* - \frac{dt}{\rho} \left(\frac{\phi_e - \phi_w}{dx} \right), \quad v_p^{n+1} = v_p^* - \frac{dt}{\rho} \left(\frac{\phi_n - \phi_s}{dy} \right), \quad (62)$$

where the subscripts are explained in Fig. 20(b) and (c). Using the pressure cell in Fig. 20(a), ee then discretize the conservation of mass equation as

$$\frac{u_e^{n+1} - u_w^{n+1}}{dx} + \frac{v_n^{n+1} - v_s^{n+1}}{dy} = 0.$$
 (63)

Substituting relations (62) into the above, we find the discrete Poisson equation

$$\frac{1}{dx} \left(\frac{\phi_E - \phi_P}{x_E - x_P} - \frac{\phi_P - \phi_W}{x_P - x_W} \right) + \frac{1}{dy} \left(\frac{\phi_N - \phi_P}{y_N - y_P} - \frac{\phi_P - \phi_S}{y_P - y_S} \right) \\
= \frac{\rho}{dt} \left(\frac{u_e^* - u_w^*}{dx} + \frac{v_n^* - v_s^*}{dy} \right).$$
(64)

Using ghost nodes, we apply the discrete Poisson equation on boundary cells, such as that sketched in Fig. 21. The Neumann conditions for the two boundaries of this corner cell are then applied as

$$\frac{\phi_P - \phi_W}{dx} = 0, \quad \frac{\phi_P - \phi_S}{dy} = 0. \tag{65}$$

Note that with all Neumann conditions, ϕ is only defined up to a constant. To produce a non-singular matrix equation, we fix the

constant using a scalar Lagrange multiplier λ . Specifically, if $A\phi=b$ represents the matrix problem generated by the Poisson equation and Neumann boundary conditions, we augment the matrix as

$$\begin{bmatrix} A & 1 \\ q & 0 \end{bmatrix} \begin{bmatrix} \phi \\ \lambda \end{bmatrix} = \begin{bmatrix} b \\ 0 \end{bmatrix}, \tag{66}$$

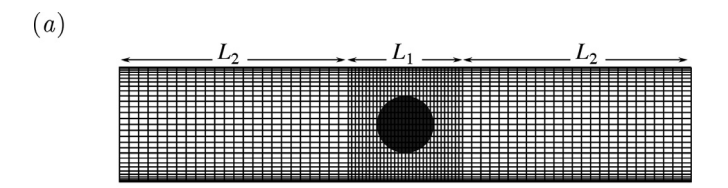
where q is a row of length $(N_x+2)(N_y+2)$ zeros, except for one entry set to unity. This sets ϕ equal to unity at one of the grid points. After solving, we confirm that $\lambda=0$ to machine precision. In all cases, we find that mass conservation is indeed satisfied to machine precision.

Appendix C. Grid independence studies

The simulations of Section 3.3 are performed using N_x equispaced cells in the x-direction. The cells are concentrated in the y-direction near the membrane and outer walls by setting the y-coordinates of the horizontal faces to

$$y_i = \pm (h/2)(1 + \cos(\pi i/N), \quad i = 0, 1, ..., N_y,$$
 (67)

where the positive sign is used in the feed, and the negative is used in the distillate. These are simply the Gauss-Lobatto-Chebyshev points mapped to the interval $y \in [0, h]$ and $y \in [-h, 0]$. For the simulations of Section 5, we refine the grid near the cylinder by decomposing the x-direction into three sections, as demonstrated in Fig. 22(a). A core section of length $L_1 = H$ is centered



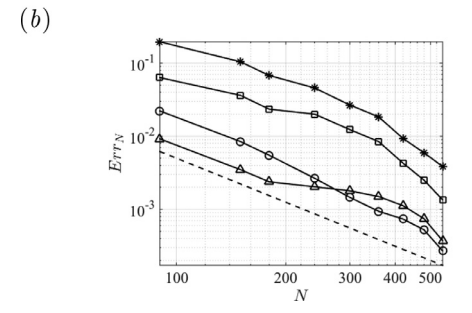


Fig. 22. (a) Demonstration of a channel grid for which $N_1 = 32$, $N_2 = 24$, and $N_y = 30$. (b) Variation of Err_N with N_x for u (squares), v (asterisks), c (circles) and T (triangles). The dashed line shows $1/N^2$.

about the cylinder, and has N_1 equispaced cells in the *x*-direction. The inlet and outlet sections each have a length $L_2 = (L - L_1)/2$ and N_2 equispaced cells.

To demonstrate our mesh independence studies, we consider here the simulation of a DCMD system with a spacer on the centerline of each channel. We set the system dimensions to H=2 mm, L=20 mm, and $D_c=0.6$ mm, producing the blockage ratio $\beta=0.3$. The operating conditions are set to $T_{in}^f=80\,^\circ$ C, $T_{in}^d=20\,^\circ$ C, $C_{in}=100$ g/L, and $U_{in}=0.021$ m/s. This produced a subcritical case for which the flow fields can be integrated to steady state. We fix the ratio $N_x/N_y=3$ and varied N_x and N_y between $90 \le N_x \le 600$ and $30 \le N_y \le 200$, respectively. We also fix the ratio $N_1/N_2=1/4$, to force 20% of the N_x cells in the core region L_1 . Simulations were run to steady-state, after which the spatial error was evaluated using the result at $(N_x, N_y)=(600, 200)$ as the exact solution. Fig. 22(b) shows the error is below 1% when $N_x>400$.

For cases with unsteady vortex shedding, we leverage the fact that v, T, and c are remarkably steady on the membrane surface. We consequently repeat the above procedure measuring the error with respect to these fields on the membrane surface. To determine the time step dt for unsteady cases, we first set dt to the maximum allowable value for which the code is numerical stable. We then compare dt to the computed period of oscillation $t_p = 1/f$ and ensure that $t_p/dt > 1000$.

Appendix D. Outlet performance studies

To explore the outlet conditions in the context of large-scale vortical flow structures, we considered flow over a cylinder in a planar channel flow. Varying the blockage ratio and cylinder position relative to the channel centerline allows us to generate a wide range of steady and unsteady vortical structures. Fig. 23 shows two simulations performed of a channel flow with Re = 320 and blockage ratio $\beta = 0.5$. The cylinder has been placed closer to the upper wall. In this case, Zovatto and Pedrizzetti [55] have shown that the asymmetry stabilizes vortex shedding and produces elongated vortical structures behind the cylinder and along the upper wall. Fig. 23 shows the results of two simulations in which the cylinder was placed three diameters from the channel inlet. The simulation in panel (a) uses a short downstream length that cuts through the vortex attached to the upper wall. The simulation in panel (b) shows a second simulation using a longer domain that allows the near-wall vortex to close well upstream from the outlet. Comparing the streamlines of the two simulations shows excellent agreement.

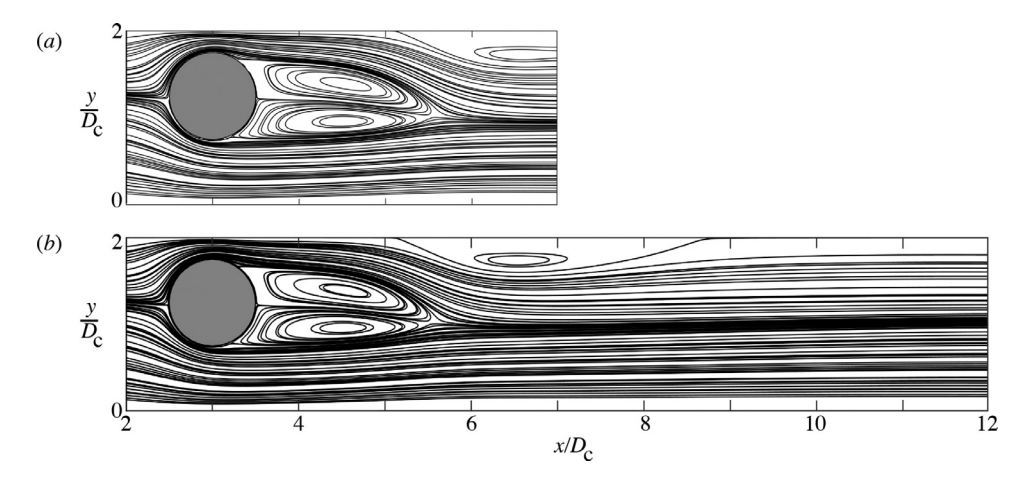


Fig. 23. Comparison of two simulations of a channel flow with Re = 320 and blockage ratio $\beta = 0.5$ using a short (a) and long (b) domain. See discussion in text.

References

- [1] Alkhudhiri A, Darwish N, Hilal N. Membrane distillation: a comprehensive review. Desalination 2012;287:55.
- [2] Hickenbottom KL, Cath TY. Comparative study of brine management technologies for desalination plants. J Memb Sci 2014;454:426.
- [3] Bouchrit R, Boubakri A, Hafiane A, Bouguecha AAT. Direct contact membrane distillation: capability to treat hyper-saline solution. Desalination 2015;376:117.
- [4] Lou J, Vanneste J, DeCaluwe SC, Cath TY, Tilton N. Computational fluid dynamics simulations of polarization phenomena in direct contact membrane distillation. J Membr Sci 2019;591:117150.
- [5] Vane LM. Review: water recovery from brines and salt-saturated solutions: operability and thermodynamic efficiency considerations for desalination technologies. J Chem Technol Biotechnol 2017;92(10):2506–18.
- [6] Fimbres-Weihs G, Wiley D. Review of 3D CFD modeling of flow and mass transfer in narrow spacer-filled channels in membrane modules. Chem Eng Process 2010;49(7):759–81.
- [7] Tamburini A, Renda M, Cipollina A, Micale G, Ciofalo M. Investigation of heat transfer in spacer-filled channels by experiments and direct numerical simulations. Int J Heat Mass Transf 2016;93:1190–205.
- [8] Chorin AJ. On the convergence of discrete approximations to the Navier-Stokes equations. Math Comput 1969;23:341–53.
- [9] Temam R. Sur l'approximation des la solution des équations de Navier-Stokes par la méthode des pas fractionnaires II. Arch Ration Mech Anal 1969;33:377–85.
- [10] Li F, Meindersma W, de Haan A, Reith T. Novel spacers for mass transfer enhancement in membrane separations. J Memb Sci 2005;253(1):1–12. doi:10.1016/j.memsci.2004.12.019.
- [11] Schwinge J, Wiley D, Fletcher D. A CFD study of unsteady flow in narrow spacer-filled channels for spiral-wound membrane modules. Desalination 2002;146(1):195–201.
- [12] Ahmad A, Lau K. Impact of different spacer filaments geometries on 2d unsteady hydrodynamics and concentration polarization in spiral wound membrane channel. J Memb Sci 2006;286(1):77–92.
- [13] Alexiadis A, Wiley DE, Fletcher DF, Bao J. Laminar flow transitions in a 2d channel with circular spacers. Ind Eng Chem Res 2007;46:5387–96.
- [14] Koutsou C, Yiantsios S, Karabelas A. Direct numerical simulation of flow in spacer-filled channels: effect of spacer geometrical characteristics. J Memb Sci 2007;291(1):53–69. doi:10.1016/j.memsci.2006.12.032.
- [15] Santos J, Geraldes V, Velizarov S, Crespo J. Investigation of flow patterns and mass transfer in membrane module channels filled with flow-aligned spacers using computational fluid dynamics (CFD). | Memb Sci 2007;305(1):103–17.
- [16] Lau K, Bakar MA, Ahmad A, Murugesan T. Feed spacer mesh angle: 3D modeling, simulation and optimization based on unsteady hydrodynamic in spiral wound membrane channel. J Memb Sci 2009;343(1):16–33.
- [17] Mojab SM, Pollard A, Pharoah JG, Beale SB, Hanff ES. Unsteady laminar to turbulent flow in a spacer-filled channel. Flow Turbul Combust 2014;92(1):563–77.
- [18] Ponzio FN, Tamburini A, Cipollina A, Micale G, Ciofalo M. Experimental and computational investigation of heat transfer in channels filled by woven spacers. Int J Heat Mass Transf 2017;104:163–77.
- [19] Williamson CHK. Vortex dynamics in the cylinder wake. Annu Rev Fluid Mech 1996;28(1):477–539.
- [20] Sahin M, Owens RG. A numerical investigation of wall effects up to high blockage ratios on two-dimensional flow past a confined circular cylinder. Phys Fluids 2004:16(5):1305–20.
- [21] Haidari A, Heijman S, van der Meer W. Optimal design of spacers in reverse osmosis. Sep Purif Technol 2018;192:441–56. doi:10.1016/j.seppur.2017.10.042.
- [22] Bolanos SJ, Vernescu B. Derivation of the Navier slip and slip length for vis-

- cous flows over a rough boundary. Phys Fluids 2017;29(5):057103. doi:10.1063/
- [23] Sani R, Shen J, Pironneau O, Gresho P. Pressure boundary condition for the time-dependent incompressible Navier-Stokes equations. Int J Numer Methods Fluids 2006;50(6):673–82.
- [24] Vanneste J, Bush JA, Hickenbottom KL, Marks CA, Jassby D, Turchid CS, et al. Novel thermal efficiency-based model for determination of thermal conductivity of membrane distillation membranes. J Membr Sci 2018;548:298–308.
- [25] Schofield RW, Fane AG, Fell CJD. Heat and mass transfer in membrane distillation. J Membr Sci 1987;33:299–313.
- [26] Yu H, Yang X, Wang R, Fane AG. Numerical simulation of heat and mass transfer in direct membrane distillation in a hollow fiber module with laminar flow. J Membr Sci 2011;384:107–16.
- [27] Smith JM, Ness HCV. Introduction to chemical engineering thermodynamics. McGraw-Hill; 1975.
- [28] Hitsov I, Maere T, Sitter KD, Dotremont C, Nopens I. Modelling approaches in membrane distillation: acritical review. Sep Purif Rev 2015;142:48–64.
- [29] Leal LG. Advanced transport phenomena: fluid mechanics and convective transport processes. Cambridge University Press; 2007.
- [30] Ferziger JH, Peric M. Computational methods for fluid dynamics. Springer-Verlag Berlin Heidelberg; 2002.
- [31] Bell JB, Colella P, Glaz HM. A second-order projection method for the incompressible Navier-Stokes equations. J Comput Phys 1989;85(2):257–83.
- [32] Brown DL, Cortez R, Minion ML. Accurate projection methods for the incompressible Navier-Stokes equations. J Comput Phys 2001;168(2):464-99. doi:10.1006/jcph.2001.6715.
- [33] Guy RD, Fogelson AL. Stability of approximate projection methods on cell-centered grids. J Comput Phys 2005;203(2):517–38.
- [34] Rempfer D. On boundary conditions for incompressible Navier-Stokes problems. Appl Mech Rev 2006;59(3):107–25.
- [35] Guermond J, Minev P, Shen J. An overview of projection methods for incompressible flows. Comput Methods Appl Mech Eng 2006;195(44):6011–45.
- [36] Tilton N, Serre E, Martinand D, Lueptow RM. A 3D pseudospectral algorithm for fluid flows with permeable walls. application to filtration. Comput Fluids 2014;93:129–45.
- [37] Pauley L. A numerical study of unsteady laminar boundary layer separation. Stanford University; 1988.
- [38] Probstein RF. Physicochemical hydrodynamics. John Wiley & Sons; 1994.
- [39] Fadlun E, Verzicco R, Orlandi P, Mohd-Yusof J. Combined immersed-boundary finite-difference methods for three-dimensional complex flow simulations. J Comput Phys 2000;161(1):35–60.
- [40] Majumdar S, Iaccarino G, Durbin P. Rans solvers with adaptive structured boundary non-conforming grids. Center Turbul Res Annu Res Briefs 2001:353–66
- [41] Balaras E. Modeling complex boundaries using an external force field on fixed cartesian grids in large-eddy simulations. Comput Fluids 2004;33(3):375–404.
- [42] Pacheco-Vega A, Pacheco JR, Rodi T. A general scheme for the boundary conditions in convective and diffusive heat transfer with immersed boundary methods. J Heat Transf 2007;129(11):1506–16.
- [43] Mittal R, Dong H, Bozkurttas M, Najjar F, Vargas A, von Loebbecke A. A versatile sharp interface immersed boundary method for incompressible flows with complex boundaries. J Comput Phys 2008;227(10):4825–52.
- [44] Luo K, Zhuang Z, Fan J, Haugen NEL. A ghost-cell immersed boundary method for simulations of heat transfer in compressible flows under different boundary conditions. Int J Heat Mass Transf 2016;92:708–17.
- [45] Luo K, Zhuang Z, Fan J, Haugen NEL. A ghost-cell immersed boundary method for simulations of heat transfer in compressible flows under different boundary conditions. Int J Heat Mass Transf 2016;92:708–17.
- [46] Yousefzadeh M, Battiato I. High order ghost-cell immersed boundary method for generalized boundary conditions. Int J Heat Mass Transf 2019;137:585–98.

- [47] Qin Z, Delaney K, Riaz A, Balaras E. Topology preserving advection of implicit interfaces on cartesian grids. J Comput Phys 2015;290:219–38.

 [48] Finn J, Apte SV. Relative performance of body fitted and fictitious domain sim-
- ulations of flow through fixed packed beds of spheres. Int J Multiph Flow 2013:56:54-71.
- [49] Patankar S. Numerical heat transfer and fluid flow. Hemisphere Publishing Corporation; 1980.
- [50] Lawson KW, Lloyd DR. Membrane distillation. J Membr Sci 1997;124:1–25.
 [51] Prosperetti A. Boundary conditions at liquid-vapor interface. Meccanica 1979;14:34–47.
- [52] Whitaker S. The method of volume averaging. Klumer Academic Publishers;
- [53] Jamet D, Chandesris M. On the intrinsic nature of jump coefficients at the interface between a porous medium and a free fluid region. Int J Heat Mass Transf 2009;52:289–300.
- [54] Roe PL. Characteristic-based schemes for the euler equations. Ann Rev Fluid Mech 1986;18:337-65.
- [55] Zovatto L, Pedrizzetti G. Flow about a circular cylinder between parallel walls. J Fluid Mech 2001;440:1-25. doi:10.1017/S0022112001004608.